Aviation-induced cirrus and radiation changes at diurnal timescales

Ulrich Schumann[1] and Kaspar Graf[1]

Received 25 July 2012; revised 8 January 2013; accepted 14 January 2013.

[1] The radiative forcing from aviation-induced cirrus is derived from observations and models. The annual mean diurnal cycle of airtraffic in the North Atlantic region exhibits two peaks in early morning and afternoon with different peak times in the western and eastern parts of the North Atlantic region. The same "aviation fingerprint" is found in 8 years (2004–2011) of Meteosat observations of cirrus cover and OLR. The observations are related to airtraffic data with linear response models assuming the background atmosphere without aviation to be similar to that observed in the South Atlantic. The change in OLR is interpreted as aviation-induced longwave radiative forcing (LW RF). The data analysis suggests an LW RF of about 600–900 mW m^{-2} regionally. A detailed contrail cirrus model for given global meteorology and airtraffic in 2006 gives similar results. The global RF is estimated from the ratio of global and regional RF as derived from three models. The extrapolation implies about 100–160 mW m^{-2} global LW RF. The models show large differences in the shortwave/longwave RF-magnitude ratio. One model computes a ratio of 0.6, implying an estimate of global net RF of about 50 mW m^{-2} (40–80 mW m^{-2}). Other models suggest smaller ratios, with less cooling during day, which would imply considerably larger net effects. The sensitivity of the results to the accuracy of the observations, traffic data, and models and the estimated background is discussed.

Citation: Schumann, U., and K. Graf (2013), Aviation-induced cirrus and radiation changes at diurnal timescales, *J. Geophys. Res. Atmos.*, *118*, doi:10.1002/jgrd.50184.

1. Introduction

[2] Aircraft emit gases and particles and cause contrails contributing to radiative forcing (RF) of climate change [*Fahey et al.*, 1999]. Aviation-induced cirrus (AIC) changes contribute possibly the largest part to RF from aviation [*Sausen et al.*, 2005; *Lee et al.*, 2009]. Contrails are visible from ground, and linear contrails can be identified in satellite data [*Schumann and Wendling*, 1990; *Bakan et al.*, 1994; *Minnis et al.*, 1998, 2005; *Mannstein et al.*, 1999; *Palikonda et al.*, 2005; *Iwabuchi et al.*, 2012]. "Linear contrail models" diagnose the cover by line-shaped contrails from the product of contrail formation potential (frequency of an air mass being suitable for contrail formation) and airtraffic density (ATD), with calibration to regional satellite observations of linear contrail cover (LiCC) [*Sausen et al.*, 1998; *Ponater et al.*, 2002; *Marquart et al.*, 2003; *Rap et al.*, 2010; *Frömming et al.*, 2011]. Estimates of global annual mean values of visible and total contrail coverage vary over a considerable range [*Rap et al.*, 2010; *Frömming et al.*, 2011] and the RF estimates for given contrail cover, optical depth, and optical properties vary from 0.3 to 25 mW m^{-2} [*Meerkötter et al.*, 1999; *Kärcher et al.*, 2010]. Linear contrails develop into contrail cirrus which are difficult to discriminate from natural (nonaviation) clouds [*Atlas et al.*, 2006]. AIC cover amounts were estimated from long-term trend differences of cirrus cover (CC) observed in regions with high and low airtraffic densities, though with uncertainty in attribution of the observed changes to aviation as single cause [*Boucher*, 1999; *Fahey et al.*, 1999; *Zerefos et al.*, 2003; *Minnis et al.*, 2004; *Stubenrauch and Schumann*, 2005]. An RF of 30 mW m^{-2} (10–80 mW m^{-2}) from these changes was derived using estimated optical properties of the additional CC [*Stordal et al.*, 2005]. A recently developed global contrail cirrus model computed an RF of 38 mW m^{-2} without and 31 mW m^{-2} with feedback of water vapor reduction by contrails on cirrus formation [*Burkhardt and Kärcher*, 2011]. Aerosol-cirrus models compute increases and decreases of CC and RF values, depending on ice nucleation modeling, with possibly large but uncertain magnitudes [*Liu et al.*, 2009; *Penner et al.*, 2009; *Hendricks et al.*, 2011]. The computed AIC cover and RF values could be compared with observations only indirectly because of missing observations.

[3] Recently, we derived the CC in a North Atlantic region (NAR) [*Graf et al.*, 2012] from day and night Meteosat Second Generation (MSG) infrared observations [*Schmetz et al.*, 2002]. An "aviation fingerprint" occurs in the diurnal cycle of cirrus properties due to a special diurnal cycle of airtraffic in this region: The regional traffic density versus UTC time of day exhibits a double wave with eastbound

[1]Deutsches Zentrum für Luft- und Raumfahrt, Institut für Physik der Atmosphäre, Oberpfaffenhofen, Germany.

Corresponding author: U. Schumann, Deutsches Zentrum für Luft- und Raumfahrt, Institut für Physik der Atmosphäre, Oberpfaffenhofen, Germany. (ulrich.schumann@dlr.de)

2169-897X/13/10.1002/jgrd.50184

traffic across the Atlantic peaking in the morning and westbound traffic peaking in the afternoon. Traffic peaks are further separated in time in the west part (W) and closer together in the east part (E) of the NAR because morning eastbound flights first arrive in W and afternoon westbound flights first arrive in E. The annual mean diurnal cycle of CC shows a similar fingerprint, in spite of large day-to-day variability. The cirrus pattern cannot be explained by the diurnal solar cycle from Earth rotation. We assume that anthropogenic changes besides from aviation are small at diurnal timescales over the remote oceanic regions. Hence, the cirrus fingerprint is likely caused by AIC. For quantification of AIC contributions, CC without aviation in that region was assumed to be either constant or similar to medium-range numerical weather forecast of natural cirrus in the North Atlantic, or similar to the observed CC in the corresponding remote South Atlantic region (SAR). The AIC cover was approximated by a linear model of delayed cover response to given ATD. The model gave best approximation to observations for delay times of 2.3–4.1 h and implied an AIC contribution to CC in the North Atlantic traffic corridor of 1–2% of the regional area, far more than the also observed LiCC.

[4] Here, we extend this approach to determine the aviation-induced longwave (LW) RF in NAR. For this purpose, we use regional OLR data in addition to CC as derived from 8 years of geostationary MSG infrared data with recently developed methods [*Krebs et al.*, 2007; *Ewald et al.*,

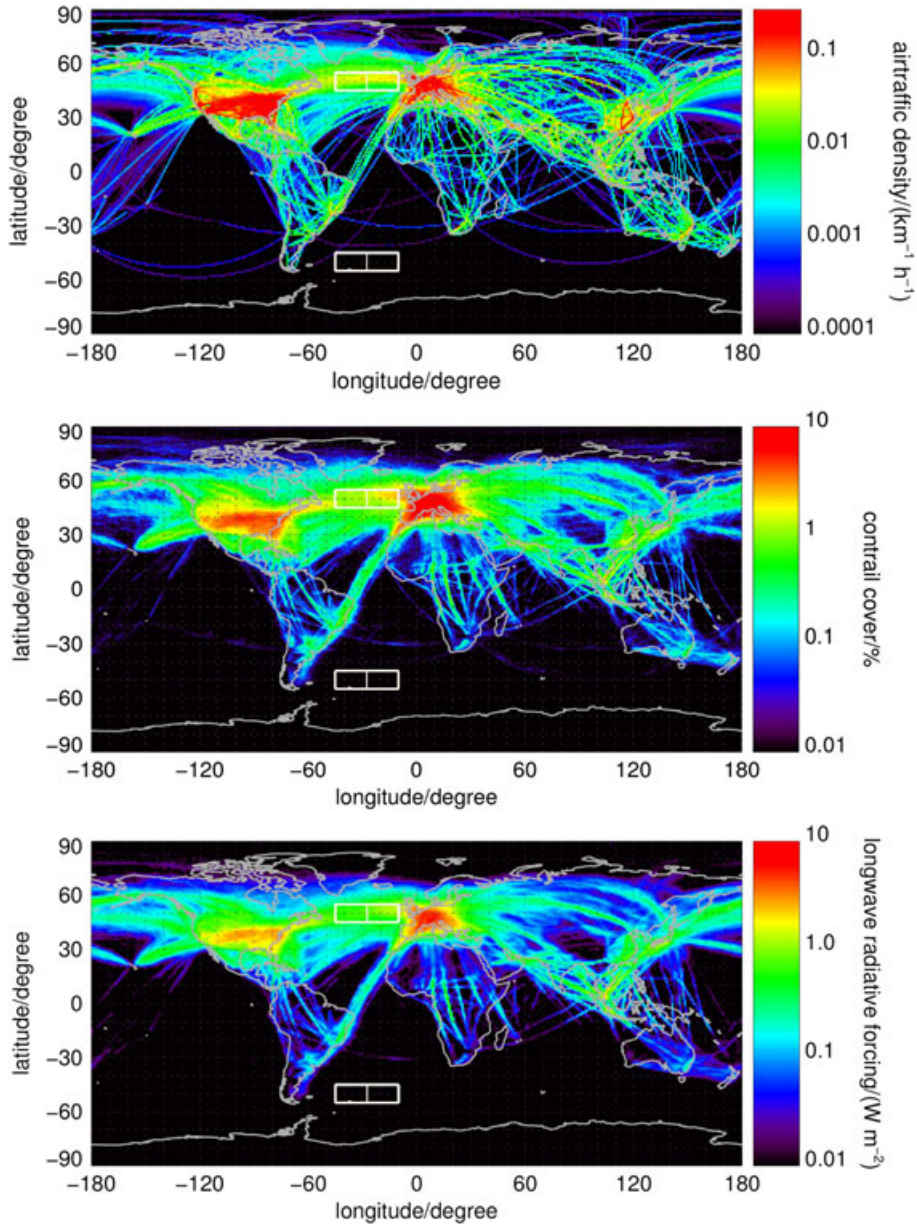

Figure 1. Top: annual mean global airtraffic density distribution; middle: cover of contrails with optical depth (at 550 nm) larger than 0.1; bottom: longwave radiative forcing. The plots show mean CoCiP results for 2006 meteorology and traffic data versus geographical longitude and latitude. White boxes identify the North Atlantic region (NAR), the South Atlantic region (SAR), and its western and eastern half parts.

2012; *Vazquez-Navarro et al*., 2012]. Similar methods are in operational use [*Schulz et al*., 2009]. The methods offer high spatial (5 km in NAR) and temporal (15 min) resolution, day and night.

[5] In addition to linear response models, the AIC is simulated with a recently developed Contrail Cirrus Prediction (CoCiP) model. CoCiP simulates the lifecycles of contrails from their formation behind individual aircraft until final dissipation for given meteorology and given aircraft and waypoint data. The model approximates the physics of contrail formation, advection, shear and turbulence-driven spreading and mixing with ambient air, and sublimation or sedimentation with a two-moment ice microphysics plume-bulk model. From the results, CC changes and RF are computed regionally and globally [*Schumann*, 2012; *Schumann et al*., 2012]. The model is applied to data for the year 2006.

[6] In addition, observed regional RF values are extrapolated globally using model results on the regional to global RF ratio. Besides CoCiP, also previously published linear contrail and contrail cirrus model results are used for this purpose.

[7] As explained before, we interpret the observed cover and OLR changes in terms of contrail cirrus changes. However, it should be noted that the satellite observations are not specific to contrails but include contributions from all other radiation effects. This may include, if present, the effects of soot and aircraft-induced aerosol changes, aerodynamic contrails [*Kärcher et al*., 2009; *Gierens et al*., 2009], and water vapor emissions. Also, air composition changes (such as ozone) at diurnal timescales due to other gaseous emissions (nitrogen oxides) contribute to the observed OLR changes. Aviation effects at longer timescales cannot be identified from the diurnal cycles.

2. Observation and Model Simulation Methods and Data

2.1. North and South Atlantic Regions

[8] The observations cover the NAR at 45°W−10°W, 45°N−55°N and its mirror region in the SAR at 45°W−10°W, 45°S−55°S. The NAR includes a large fraction of the North Atlantic flight corridor and is within the visibility range of MSG (satellite zenith angles 53°–76°), while the SAR is remote from main traffic routes, Figure 1. As discussed in section 4.1, we assume that the SAR may serve as an approximation for a hypothetical NAR without aviation. Because of systematic differences in airtraffic scheduling, the W and E parts of these regions are also considered separately.

2.2. Airtraffic Density

[9] Vertically integrated airtraffic data above 6.1 km with 0.25° spatial resolution and 15 min time resolution were obtained from the European Organization for the Safety of Air Navigation (EUROCONTROL) for a North Atlantic-European region including NAR for 2004 [*Graf et al*., 2012]. In addition, a global data set was set up by the Federal Aviation Administration (FAA) with support from Volpe National Transportation Systems Center for 2006. This "Aviation Climate Change Research Initiative (ACCRI) data set" was made available to us within the FAA ACCRI project [*Brasseur and Gupta*, 2010; *Wilkerson et al*., 2010]. The data set provides the sequences of spatial and temporal waypoint coordinates of the more than 80,000 commercial flights per day. Here, we consider all flight segments above 3.8 km (650 hPa) altitudes.

[10] For NAR, about 80% of the route data is based on pilot reported positions, about 10% is constructed from flight plan information, and the remainder from great-circle routes. From comparison of 140 instrumented airliner flight routes from Measurements of Ozone and Water Vapor aboard Airbus In-service Aircraft (MOZAIC) [*Marenco et al*., 1998] with the corresponding flight route reported in these ACCRI data, we found perfect spatial agreement for the pilot-reported ACCRI data (130 flights) and some spatial discrepancies for the flights labeled as "plan data" in the ACCRI data (10 flights). There were no great-circle routes in this 140 flights sample. For both sources of flights, for the pilot-reported ones and the planned routes, we observe differences in the temporal coordinates: By comparing the crossing time at 40°W longitude, ACCRI time is, on average of all 140 flights, 0.42 ± 0.59 h later than the MOZAIC-reported time (0.29 ± 0.54 h at 20°W, 0.65 ± 0.67 h at 40°W). This time uncertainty is taken into account in model simulations, see below.

2.3. Cirrus Cover

[11] For day and night cirrus detection, we use the Meteosat Cirrus Detection Algorithm version 2 (MeCiDA2) [*Ewald et al*., 2012] with data of the Spinning Enhanced Visible and Infrared Imager (SEVIRI) operating on the geostationary MSG satellites Meteosat-8/9 since February 2004/December 2007. MeCiDA2 combines morphological and multispectral threshold tests and detects ice clouds making use of seven SEVIRI channels between 6.2 and 13.4 μm. MeCiDA2 provides a binary cirrus mask (0 or 1) at about 5 km resolution in NAR every 15 min. Scene animations are available in *Vazquez-Navarro et al*. [2012]. The method has been validated by comparison with MODIS cirrus observations. The two methods provide similar regional mean cover within a few percent differences. The cover detection efficiency was estimated to be above 50% above a cirrus optical depth (550 nm) threshold of about 0.1–0.25 [*Vazquez-Navarro et al*., 2012]. This was confirmed in validation studies [*Bugliaro et al*., 2012; *Kox*, 2012] by comparison to airborne high spectral resolution lidar measurements of the extinction profile of thin cirrus and by comparison to the optical depth of thin cirrus derived from backscatter profiles measured by the CALIPSO mission [*Winker et al*., 2010]. MeCiDA2 results are compared to ECMWF CC in section 4.2. In addition, we use estimates of LiCC as identified from the same set of SEVIRI data by a Contrail Detection Algorithm [*Mannstein et al*., 1999; *Graf et al*., 2012].

2.4. Outgoing Longwave Radiation

[12] The OLR at top of the atmosphere is derived from the same SEVIRI data, using the Rapid Retrieval of Upwelling Fluxes from MSG/SEVIRI (RRUMS) method [*Vazquez-Navarro et al*., 2012]. This method provides the net outgoing LW irradiance from a linear combination of brightness temperatures of SEVIRI channels at the same time and space resolution as MeCiDA2. The method has been validated by comparison with irradiance observations from the CERES on the polar orbiting satellite TERRA [*Loeb et al*., 2009] and by the GERB instrument [*Harries et al*., 2005]. GERB is operated

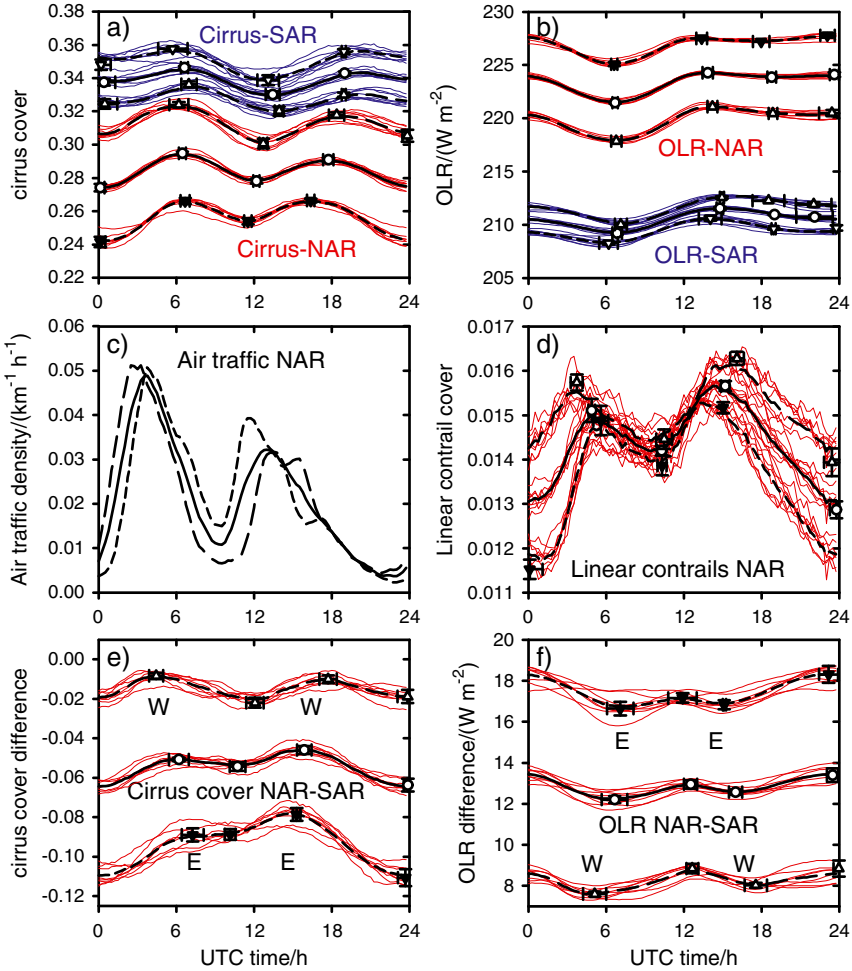

Figure 2. Eight-year mean diurnal cycles for (a) cirrus cover, (b) OLR in the total regions (NAR and SAR) and their west/east parts (W/E), (c) airtraffic density (ATD) (from EUROCONTROL data), (d) linear contrail cover (LiCC), (e) cirrus cover differences, and (f) OLR differences between NAR and SAR. The line coding separates between annual results (colored lines: red for NAR and blue for SAR), 8-year mean values (thick curves), west (W, long dashed), east (E, short dashed), and the total regions (full curves). Significant points identify the minima/maxima mean of the annual mean diurnal cycles and their timing, with standard deviations.

together with SEVIRI on MSG. RRUMS has been shown to be a reliable method to calculate the OLR, and the OLR agreed better than 1% with CERES on average over a set of test cases. The spatial resolution of SEVIRI is remarkably better than that of CERES (20 km) or GERB (45 km). The temporal resolution is the same as GERB (15 min). Validation data for NAR and SAR will be discussed in section 4.2.

2.5. Data Analysis Methods

[13] For the analysis of diurnal cycles, the discrete times t since 00 UTC 1 February 2004 are decomposed as $t = t_i + (d-1)\cdot 24\ \mathrm{h} + (\mathrm{y}-1)\cdot 364$ days, for daytime $t_i = (i-1)\cdot\Delta t$, $\Delta t = 15$ min, $i = 1, 2, ..., I = 96$, day $d = 1, \ldots, D = 364$, and year $y = 1, \ldots, Y = 8$, including 2912 consecutive days until 21 January 2012.

[14] The use of 364 days per "year" allows for division into equal-sized annual samples and into two or four subsamples of equal sizes for each year. Results for $D = 365$ days per year, with 8 more days, or for 2922 instead of 2912 days show negligible differences.

[15] Regional mean values $c(t_i,d,y)$ for CC, and similarly for LiCC and OLR, are averages of the Meteosat data for NAR and SAR and their subregions W and E, at discrete times every 15 min. The annual mean diurnal cover cycles are computed by averaging over all days after subtraction of interannual variability [*Graf et al.*, 2012],

$$C(t_i, y) = \langle c(t_i, d, y)\rangle_d - \left[\langle c(t_i, d, y)\rangle_{t_i,d} - \langle c(t_i, d, y)\rangle_{t_i,d,y}\right]. \quad (1)$$

[16] Here, angular brackets with index define arithmetic mean values with respect to the indexed variable.

[17] The results are shown in Figure 2. In addition, we consider deviations of the diurnal cycle from its mean for each year, i.e.,

$$C'(t_i, y) := C(t_i, y) - \langle C(t_i, y)\rangle_{t_i}. \quad (2)$$

[18] Deviations from periodicity occur in mean diurnal cycles for finite nonperiodic time series but are negligible in the 8-year mean.

2.6. Linear Response Model

[19] As in *Graf et al.* [2012], a linear response model is used to estimate timescales τ and the AIC contributions to CC, LiCC, and, here, also OLR. Subsequently, we summarize the approach for C being cover. The response model $C_m(t_i)$ assumes that the annual mean diurnal CC is the sum of the background cirrus $C_0(t_i)$ and an AIC contribution $C_A(t_i)$. The background part is split into a constant mean background and its diurnal deviation, $C_0(t_i) = B + b(t_i)$. The AIC contribution is assumed to be proportional to ATD $a(t_i)$ in the past according to a response function $r(t_i)$ with adjustable amplitude A and timescale τ,

$$C_m(t_i) = B + b(t_i) + C_A(t_i), \tag{3}$$

$$C_A(t_i) = Af(t_i), f(t_i) = \int_{-\infty}^{t_i} a(\hat{t}) r(t_i - \hat{t}) d\hat{t}. \tag{4}$$

[20] The response function defines the cover response to a δ-pulse traffic forcing. Among others [*Graf et al.*, 2012], we use

$$r(t) = \left(4t/\tau^2\right)\exp(-2t/\tau). \tag{5}$$

[21] It is defined so that $\int_0^\infty r(t)dt = 1$, and $\tau = \int_0^\infty tr(t)dt$ is the delay time represented by $r(t)$. The spectral width of timescales represented by r is measured by the variance $v^2 = \int_0^\infty (t-\tau)^2 r(t)dt$, which equals $v^2 = (1/2)\tau^2$ for this response function. An increase of r with t at small times is expected because it takes some time until the initially narrow contrails become visible in Meteosat pixels [*Duda et al.*, 2001; *Mannstein and Schumann*, 2005; *Atlas et al.*, 2006]. The later exponential decay is consistent with a few available empirical frequency distributions of contrail lifetimes [*Mannstein et al.*, 2012; *Schumann*, 2012]. For the deviation $b(t_i)$ of the background part C_0 from its mean value B, we assume either of three alternatives:

$$\begin{aligned} &b(t_i) = 0, b(t_i) = \langle C_{\mathrm{SAR}}(t_i, y)\rangle_y, \\ &b(t_i) = \langle C_{\mathrm{SAR}}(t_i, y)\rangle_y + C_{\mathrm{SOT}}(t_i). \end{aligned} \tag{6}$$

The first alternative assumes constant background $C_0(t_i)$ with zero deviation $b(t_i)$. The second assumes the background deviation part $b(t_i)$ in the NAR to be as observed on average over 8 years in the SAR. The third alternative assumes that the diurnal cycle of the background equals the mean SAR observations plus a correction for climatological mean differences between NAR and SAR estimated with a solar tide model SOT, see Appendix A. For LiCC, we use the first alternative, for CC the first and the second, and for OLR all three alternatives. For LiCC, CC, and OLR, the three fit parameters B, A, and τ are determined by minimizing the RMS error χ,

$$\chi^2(y) = \left\langle \left(C(t_i, y) - C_m(t_i, y)\right)^2 \right\rangle_{t_i}. \tag{7}$$

[22] The day mean AIC(y) contributions are $< C_A(t_i, y) >_{t_i}$, see equation 4. The fit is performed separately for each year, giving Y different fit results $B(y)$, $A(y)$, and $\tau(y)$. Actually, we fit separately for the regions NAR, NAR-W, and NAR-E and average the results. Eight-year mean values of the results for AIC and τ are listed in Table 1. The fit quality is assessed by standard deviations σ because of interannual variability, fit errors χ, and Pearson's correlation coefficients ρ between $C(t_i,y)$ and $C_m(t_i)$.

[23] Technically, for fixed τ and fixed f, see equation 4, the parameters B and A enter the fit linearly. Hence, they are the solutions of linear equations with determinate $d = \langle f^2\rangle - \langle f\rangle^2$:

$$\begin{aligned} A &= [\langle f(C-b)\rangle - \langle f\rangle\langle C\rangle]/d, \\ B &= \left[\langle f^2\rangle\langle C\rangle - \langle f(C-b)\rangle\langle f\rangle\right]/d. \end{aligned} \tag{8}$$

[24] As a consequence, $\langle C_m\rangle = \langle C\rangle$, $\mathrm{AIC} = \langle \mathrm{C_A}\rangle = \mathrm{A}\langle \mathrm{f}\rangle$, $B = \langle C\rangle - \langle C_A\rangle$, and $B = -\langle C_A\rangle$ when fitting to C' values with zero mean. Hence, $\sigma(B) = \sigma(\mathrm{AIC})$, and $\sigma(A) = \sigma(\mathrm{AIC}/\langle \mathrm{f}\rangle)$. The magnitude and sign of A depends on the correlation between f and $C - b$. For given correlation, the magnitude of C_A and fit errors increase for decreasing determinate d. d becomes small for large τ^2, for small airtraffic variance $\langle a^2\rangle - \langle a\rangle^2$, and for a wide response function r with large temporal variance v^2/τ^2. The optimal fit for τ is found numerically by systematic discrete variation [*Schumann et al.*, 2012]. The fit results are independent of a linear scaling of traffic density but sensitive to time shifts or other changes of $a(t)$.

Table 1. Fit Results for Cirrus Cover CC and OLR, for Annual mean EUROCONTROL Airtraffic Density ATD and for Two Background Variants (SAR or SOT: Solar Tide-corrected SAR), on Average Over NAR, NAR-W, and NAR-E, for Delay Time τ and its Standard Deviation $\sigma(\tau)$ in h, AIC, and its Standard Deviation σ(AIC) in Area Percentage (for CC) or W m^{-2} (for OLR), Correlation Coefficient ρ, and RMS Error χ in the Same Units as AIC Cover and OLR

Field	$b(t)$	$\tau \pm \sigma(\tau)$	AIC $\pm$ σ(AIC)	ρ	χ
CC	SAR	3.72 ± 1.56	1.58 ± 0.885	0.930	0.236
OLR	SAR	2.84 ± 0.43	-0.876 ± 0.346	0.994	0.102
OLR	SAR + SOT	2.68 ± 0.56	-0.757 ± 0.333	0.994	0.098

2.7. Contrail Cirrus Simulation Model

[25] Contrail cirrus simulations are performed using the contrail cirrus model CoCiP introduced above. CoCiP is run using waypoint data from ACCRI (with 1 h delay globally) and meteorological data from the ECMWF Reanalysis Interim data [*Dee et al.*, 2011], cycle 31r2 (http://www.ecmwf.int/research/ifsdocs/CY31r1/index.html). The reanalysis data include the improved treatment of ice supersaturation [*Tompkins et al.*, 2007] for the full year 2006. We use the data at $1^\circ \times 1^\circ$ horizontal resolution with 15 pressure levels (650–100 hPa) available 3-hourly from forecast starting 00 (for 6 to 15 UTC) and 12 UTC (for 18 to 3 UTC) each day. This is a compromise between good agreement with observations (short forecast times) and well-developed ice supersaturation (long forecast times).

[26] CoCiP model results depend on various critical model parameters [*Schumann*, 2012]. Besides ambient humidity and particle loss processes, which we treat as described earlier, we found that mixing between the contrails and ambient air, as controlled by vertical diffusivity of plume air, is of particular importance. Enhanced vertical plume mixing causes geometrically thicker contrails. Thicker contrails experience enhanced

horizontal spreading by wind shear. Enhanced vertical and horizontal mixing causes larger plume cross-sections with more humidity entrained. For constant number of ice particles in the contrail, the ice particles share in a larger amount of water deposited from entrained ambient ice supersaturated air. Hence, enhanced vertical mixing causes larger cover, larger particles, larger optical depth, and larger RF. Larger particles also experience stronger sedimentation. Sedimentation contributes to further vertical spreading and shorter contrail lifetimes.

[27] It is well known that turbulence is often larger inside cirrus than in clear air, and an order of magnitude difference is well supported by measurements [*Gultepe and Starr*, 1995]. Since many contrails occur in thin cirrus [*Immler et al*., 2008; *Iwabuchi et al*., 2012], we enhance vertical plume diffusivity by a factor of 5 compared to what we used before and enhance vertical diffusivity further when radiative heating in the contrails causes convective instability [*Jensen et al*., 1998]. Radiative heating is strong in particular in thick contrails.

[28] The model computes contrail cover as the result of CC above optical depth 0.1 with contrails (partially overlapping) minus CC without contrails, every hour, during a full year. It also computes the instantaneous RF at TOA, applying an analytical model for each contrail segment for given local contrail properties and radiation fluxes at TOA as provided with the ECMWF forecast. The RF from overlapping contrails is added linearly taking cirrus above the contrails into account. The model has been tested successfully for a 1-year simulation of global RF by a homogeneously distributed contrail cirrus [*Myhre et al*., 2009; *Schumann et al*., 2012]. The computed LW RF corresponds to the observable negative change in OLR due to aviation at short time scales. Therefore, we will compare CoCiP-computed LW RF with negative OLR changes.

3. Results

3.1. The Aviation Fingerprint in Cirrus Cover and Longwave Radiation

[29] The annual mean diurnal cycles of CC and OLR on NAR and SAR, and LiCC for NAR, from 8 years of Meteosat data, are shown in Figure 2. The figure shows also the mean diurnal cycle of ATD in 2004 and the cover and OLR differences between SAR and NAR. The thin curves show the annual mean cycles, after subtraction of interannual variability of the mean values, see equation 1. The thick curves show the 8-year mean cycles. The cycles show a diurnal double wave with four extreme values, two maxima and two minima. The

Table 2. Minima/Maxima Coordinates With Standard Deviations (sd) Based on Eight Annual Results. N Denotes NAR, S Denotes SAR, and N-S is the Difference NAR-SAR

		Total domain				West part				East part			
		Time	sd (time)	Value	sd (value)	Time	sd (time)	Value	sd (value)	Time	sd (time)	Value	sd (value)
1st max	ATD	3.75		0.0489		2.50		0.0512		3.75		0.0508	
1st min	ATD	9.50		0.0108		9.50		0.0066		9.50		0.0150	
2nd max	ATD	13.00		0.0322		13.25		0.0316		11.50		0.0393	
2nd min	ATD	22.75		0.0037		21.75		0.0045		23.00		0.0023	
	CC-N	6.47	0.26	0.2948	0.0010	6.19	0.74	0.3239	0.0016	6.69	0.35	0.2662	0.0019
	CC-N	12.19	0.24	0.2782	0.0015	12.72	0.32	0.3007	0.0029	11.53	0.29	0.2540	0.0020
	CC-N	17.75	0.40	0.2909	0.0011	18.38	0.59	0.3177	0.0016	16.38	0.28	0.2664	0.0011
	CC-N	0.13	0.33	0.2741	0.0022	23.84	0.37	0.3053	0.0036	0.13	0.38	0.2415	0.0030
	CC-S	6.63	0.28	0.3463	0.0010	6.97	0.59	0.3362	0.0017	5.72	1.13	0.3576	0.0013
	CC-S	13.44	0.56	0.3301	0.0019	13.94	0.35	0.3202	0.0027	13.09	0.84	0.3388	0.0029
	CC-S	19.00	0.00	0.3430	0.0011	18.94	0.17	0.3301	0.0013	18.94	0.17	0.3559	0.0015
	CC-S	0.41	0.88	0.3375	0.0020	0.47	0.96	0.3245	0.0029	0.19	0.75	0.3481	0.0031
	CC-N-S	6.19	0.78	0.1893	0.0009	4.44	0.54	0.2316	0.0016	7.25	0.86	0.1510	0.0034
	CC-N-S	10.72	0.61	0.1857	0.0023	12.06	0.66	0.2181	0.0025	10.16	0.41	0.1513	0.0028
	CC-N-S	15.88	0.57	0.1941	0.0020	17.72	0.68	0.2300	0.0020	15.28	0.29	0.1614	0.0032
	CC-N-S	23.88	0.33	0.1730	0.0033	23.84	0.78	0.2178	0.0034	23.69	0.58	0.1250	0.0043
	LiCC-N	4.88	0.25	0.01511	0.00026	3.72	0.46	0.0157	0.0002	5.59	0.57	0.0149	0.0003
	LiCC-N	10.28	0.34	0.01420	0.00011	10.47	0.61	0.0145	0.0002	10.31	0.35	0.0139	0.0002
	LiCC-N	15.19	0.32	0.01566	0.00011	16.09	0.53	0.0163	0.0002	15.03	0.08	0.0152	0.0001
	LiCC-N	23.78	0.51	0.01287	0.00019	23.44	0.62	0.0139	0.0003	0.09	1.00	0.0115	0.0002
	OLR-N	6.69	0.21	221.47	0.09	6.78	0.40	217.84	0.14	6.63	0.25	225.06	0.17
	OLR-N	13.84	0.39	224.26	0.13	14.22	0.38	221.09	0.19	13.38	0.41	227.49	0.15
	OLR-N	18.78	0.34	223.86	0.09	18.88	0.33	220.46	0.12	17.97	0.64	227.20	0.00
	OLR-N	23.63	0.35	224.10	0.20	23.44	0.99	220.49	0.29	23.09	0.57	227.78	0.21
	OLR-S	6.84	0.35	209.20	0.12	7.13	0.47	210.04	0.13	6.19	0.73	208.28	0.13
	OLR-S	14.78	0.26	211.54	0.14	14.94	0.17	212.56	0.12	14.03	0.88	210.59	0.22
	OLR-S	19.00	0.00	210.95	0.07	18.53	1.24	212.26	0.07	18.94	0.17	209.62	0.08
	OLR-S	22.09	1.41	210.73	0.19	22.03	1.37	211.91	0.21	23.78	0.26	209.71	0.26
	OLR-N-S	6.66	0.98	12.20	0.18	5.13	0.89	7.60	0.12	7.09	1.02	16.65	0.33
	OLR-N-S	12.53	0.51	12.95	0.20	12.66	0.47	8.84	0.24	11.91	1.11	17.17	0.23
	OLR-N-S	16.00	0.50	12.57	0.13	17.56	0.85	8.02	0.12	15.13	0.13	16.83	0.22
	OLR-N-S	23.50	0.43	13.74	0.34	23.97	0.40	8.83	0.39	23.19	0.74	18.73	0.41

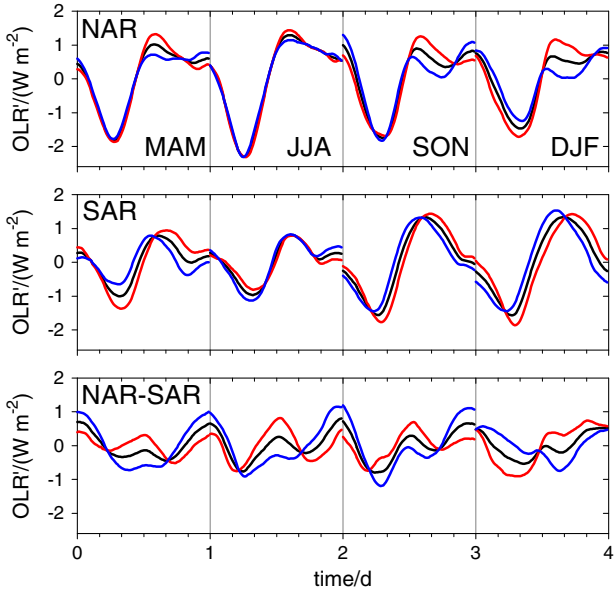

Figure 3. Seasonal mean diurnal cycle differences OLR′ (see equation 2) in NAR (top), SAR (middle) and in the NAR-SAR difference (bottom, subtracting SAR results shifted by 6 months), from OLR observations for the total domain (black) and the west (red) and east (blue) subregions. Each panel shows quarterly mean diurnal cycle results versus time of day, shifted by 1 day for each season from left to right, from March, April, May (MAM) to December, January, February (DJF).

magnitude and time coordinates of these extreme value points are computed separately for each annual mean cycle and then averaged. The coordinates, listed in Table 2, are separated by more than their standard deviations both in magnitude and time. The mean coordinates at subsequent points differ significantly at the 99.8% probability level. The cover/OLR variability would be far larger without subtraction of the mean interannual variability. The cirrus double waves are delayed in time relative to that of ATD: The time coordinates of the extreme values of OLR and CC are delayed by 3.3 h (1.8–4.5 h) and those of LiCC by 1–2 h.

[30] In NAR, the diurnal ATD cycle in Figure 2 reveals two maxima during traffic rush hours [*Graf et al.*, 2012]. Separately for the W and E halves of the NAR, the diurnal ATD cycles show a unique fingerprint of aviation, see Figure 2. Traffic in NAR first increases in the western part because of early arrivals of eastbound flights in the morning and increases about 1–2 h later in the eastern part. The westbound afternoon traffic exhibits the opposite sequence in time: it increases first in the eastern part and later in the western part.

[31] The same aviation fingerprint can be seen in annual mean CC [*Graf et al.*, 2012]. The CC double wave follows the diurnal ATD cycle with a delay time of about 3–5 h. As for ATD, the cirrus cycle peaks are further separated in time in W and closer together in E. This CC fingerprint is detectable for each individual year of CC [*Graf et al.*, 2012].

[32] The CC in SAR also shows a double wave. However, the CC double wave on SAR does not have the E-W fingerprint as ATD. Instead, the diurnal OLR cycle on SAR shows a natural diurnal cycle with a wave component migrating from east to west in time with the sun. This is consistent with the solar tide model (Appendix A) and with ECMWF results (see section 4.1). Solar tide temperature waves are caused by solar heating during day and infrared cooling [*Hagan and Forbes*, 2002, 2003]. At least over extratropical oceans, without cool cloud tops from afternoon convection, infrared cooling dominates during night and solar heating during daytime. This causes a diurnal mode of OLR with decrease of OLR during night and increase during day, in line with observations [*Comer et al.*, 2007] and models [*Slingo et al.*, 2004].

[33] The aviation fingerprint is well visible in the differences between NAR and SAR of annual mean diurnal cycles of CC and OLR, see Figures 2e and 2f. These differences exhibit signatures similar to that of ATD. The NAR-SAR difference of OLR follows CC but with opposite sign. Enhanced CC is correlated with reduced OLR. Also, the cover of linear contrails shows this pattern but with smaller temporal delay. All these properties are consistent with AIC as possible cause.

[34] The aviation fingerprint shows up for all seasons in the 8-year mean diurnal cycles, see Figure 3. Here, we plot the deviations from the daily mean values, see equation 2, which eliminates the differences between the mean values in the various regions. Similar results were shown for contrail CC and LiCC in *Graf et al.* [2012].

[35] The AIC contributions show the largest amplitudes in summer and autumn, partly because of the highest tropopause [*Wilcox et al.*, 2012], with frequent traffic in the upper troposphere [*Hoinka et al.*, 1993; *Forster et al.*, 2003], and relatively high temperatures, implying large water content for the same relative ice supersaturation, stronger sedimentation [*Schumann*, 2012], and possibly stronger radiative heating impact on contrail and cirrus dynamics. The double wave increases more quickly and shows stronger variability at noon times in SON and JJA than in the other seasons. Hence, the delay times are larger in winter than in summer.

[36] Contrail occurrence is also weather and route dependent [*Irvine et al.*, 2012]. We computed the mean diurnal cycles separately for those days where the mean humidity at flight levels (175–300 hPa) was above or below its median value (about 0.6) using ECMWF data for NAR in 2006. The diurnal cycle amplitudes (not shown here) are about twice larger for high than for low humidity.

3.2. Fit Results

[37] Table 1 lists the fit results for the AIC contributions to CC and OLR and the delay times τ. Fits were computed for several linear response functions r as described in *Graf et al.* [2012]. The best correlation between fitted and observed values is obtained for the selected response function, equation 5. Therefore, Table 1 lists the results for this response function only. For CC, the fit results depend rather weakly on the assumed background [*Graf et al.*, 2012]. Both constant and SAR backgrounds give similarly small fit errors, high correlations, and low interannual variability of the fit parameters. The true background may be in between these two, because a fit with the mean of them gives slightly smaller fit errors.

[38] However, for OLR, the solar cycle is essential for accurate fits. The SAR signal appears to provide a reasonable approximation of the NAR signal without aviation impact. It gives equally valid fits separately for the W and E parts. For OLR with this background, the results show significantly higher correlation coefficients than for constant background (0.994 instead of 0.7) and smaller approximation errors

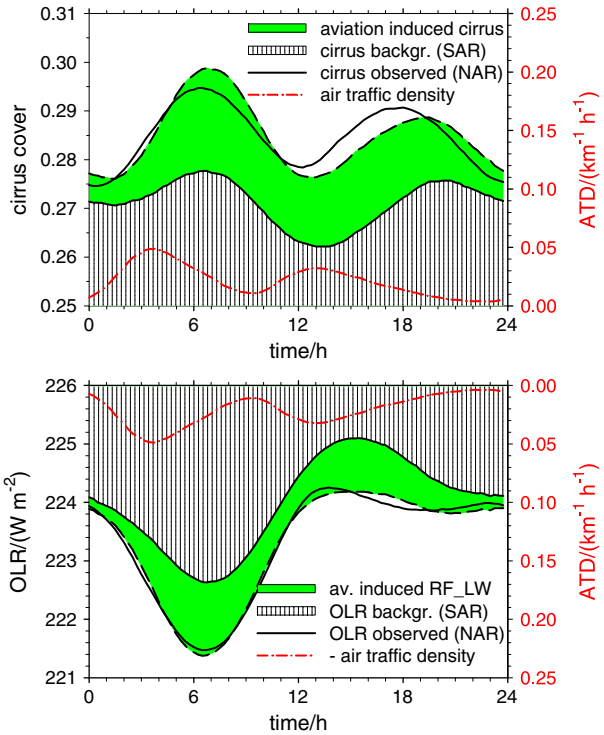

Figure 4. Aviation contributions to the diurnal cycle. Top: cirrus cover; bottom OLR. Red dash-dotted curves: airtraffic density ATD in NAR. Since cover increases with airtraffic density while OLR decreases, negative ATD is plotted in the lower panel. The full curves represent the observed cirrus cover and OLR diurnal cycles. The green areas bounded by the fit results (short dashed) of cirrus cover and OLR display the aviation-induced contributions. The AIC contributions are determined by fitting the linear response model with response function equation 5, assuming the SAR results to represent the NAR without aviation (indicated by vertically shaded areas).

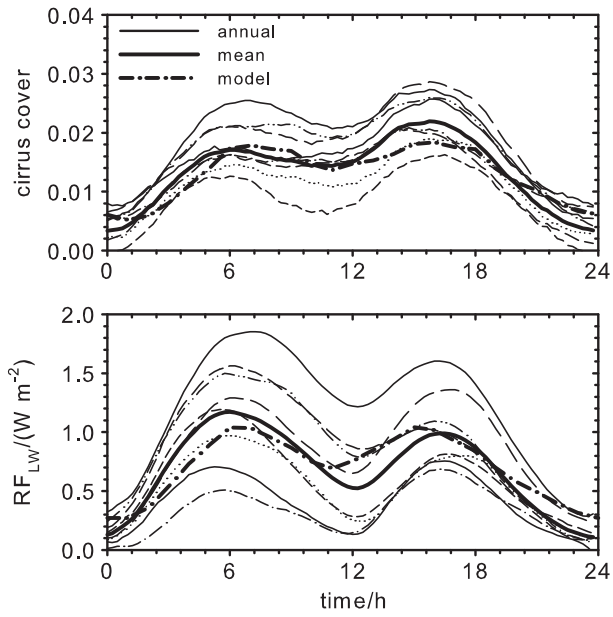

Figure 5. Diurnal cycle of cirrus cover (top) and regional LW RF (bottom) versus UTC time of day as derived from fitted observations for NAR with background as in SAR for CC and SAR-SOT for OLR, for the 8 individual years (thin full lines with different line coding for different years), for the 8-year mean (thick full), and as modeled with CoCiP for 2006 (thick dash-dotted).

(0.102 instead of 0.670 W m^{-2}). Hence, the SAR background is clearly better suited than constant background.

[39] Parts of the remaining NAR-SAR differences may be corrected with the SOT model. The SOT variant of the fit gives higher correlation. Tests with increased SOT amplitude showed no correlation improvements. Inclusion of the SOT cycle gives slightly smaller (about 15%) aviation contribution to OLR. A fit for individual months shows good correlations for all months except February and March.

[40] The fit results show positive cover changes and negative OLR changes in reasonable correlation with the airtraffic signal. The AIC contribution for cover is larger than the annual mean diurnal amplitude of CC on SAR. For OLR, the AIC contribution amounts to 37% of the SAR OLR amplitude, which is still a large contribution. The OLR is far better ($\rho > 0.99$) correlated with ATD than CC ($\rho > 0.93$), partially because of the larger amplitude of OLR but perhaps mainly because of the better physical definition of OLR compared to cover. The cover and OLR responses follow the ATD signal with about 3 h of delay, which appears plausible in view of previous (though uncertain) contrail cirrus age estimates [*Immler et al.*, 2008; *Mannstein et al.*, 2012; *Schumann*, 2012]. The delay times are definitely smaller than the 9.5 h difference between the NAR traffic peaks.

[41] Figure 4 shows the mean fit results assuming SAR background and illustrates the variations of ATD, and the AIC and OLR responses, with delays of AIC and OLR compared to ATD. The AIC cover determined this way is an order of magnitude larger than the cover by line-shaped contrails derived with a contrail detection algorithm [*Mannstein et al.*, 1999] from the same data, and shows about twice as large delay times [*Graf et al.*, 2012].

[42] Figure 5 shows fit results for individual years. For comparison with model results (see section 3.3), this figure plots the LW RF which we estimate to be equal to the negative OLR change. The curves represent, e.g., for cover, $C(t_i) - b(t_i) - B$. For cover, $b(t_i)$ refers to the 8-year mean SAR signal; for −OLR or LW RF, it includes the NAR-SAR difference estimated with the solar tide model SOT. We find positive cover and RF values for each year. The mean values of the individual fit results and the standard deviations of these mean values are $1.5 \pm 0.4\%$ for cover and 0.71 ± 0.3 for LW RF. The relative scatter is larger for RF than for cover. There is no systematic trend with the years. Note that these results are computed for fixed air traffic data. A 0.5-h shift of ATD forward in time improves the fit correlations and gives slightly larger amplitudes. The fits were computed for the same background for each year. Hence, interannual weather variations and related changes in the NAR signal without aviation are not taken into account. The RF and cover results are weakly correlated ($\rho = 0.7$) among each other. Therefore, the RF/cover ratio is reasonably robust (50 ± 18 W m^{-2}). This rather large ratio will be discussed in section 4.3. Annual mean RF and cover results are also weakly ($\rho = 0.6$–0.7) correlated

with the annual mean cover of linear contrails and with the amplitudes of mean diurnal cycles of OLR in the NAR. Hence, part of the interannual cover and RF variability seen in Figure 5 may be caused by weather variability.

[43] The fits reveal slightly shorter delay times for OLR than for CC. The shorter delay time for OLR may have several reasons (besides data uncertainties): Contrails thinner than the threshold-dependent detection limit of MeCiDA2 are not detected as clouds but may have large subvisible cover and may contribute to OLR. Also, contrails above or within already clouded regions do not change the cover but may change OLR.

[44] Table 1 suggests AIC changes in NAR at diurnal timescales of about $1.5 \pm 0.8\%$ cover, $0.77 \pm 0.34\,\mathrm{W\,m^{-2}}$ OLR, and delay times of 2.5–2.8 h for OLR. The RMS fit errors χ (about $0.1\,\mathrm{W\,m^{-2}}$) are smaller than the interannual fluctuations. The mean value uncertainty may be smaller than the standard deviation (by about $\sqrt{7} = 2.6$ for 8 independent years). Hence, we estimate the annual mean LW RF to be within 0.75 ± 0.15 or 0.6-0.9 $\mathrm{W\,m^{-2}}$ in NAR regionally.

3.3. Comparison of Fit and Contrail Cirrus Model Results

[45] CoCiP has been applied to compute the regional and global contrail cover and RF. The results are presented for comparison with the regional observations and for global extrapolation. The many details of the results, with parameter studies and comparisons to further observations, are to be described elsewhere. For illustration, Figure 1 shows the computed annual mean contrail cover distribution.

[46] The basic pattern follows the airtraffic distribution, but meteorology plays a role, as is well known. For example, cover is less than expected from traffic density in the often dry polar region and in the warm tropics. CoCiP simulates contrail advection over the contrail lifetimes. As a consequence, contrail cover is further dispersed than traffic density. The dispersion is, however, smaller than computed with a global contrail cirrus model [*Burkhardt and Kärcher*, 2011], possibly because of higher spatial resolution and smaller lifetimes in CoCiP.

[47] The mean computed cover (for optical depth larger than 0.1) is 1.3% in NAR, 5.4% over mid Europe, and 0.23% globally. The cover is practically zero in SAR. The global cover is about 2.5 times larger and optically far (about factor 5) thicker than previously computed with linear contrail models [*Marquart et al.*, 2003; *Frömming et al.*, 2011] but close to global estimates (0.24% (0.07–0.41%)) derived from regional cirrus trends [*Stordal et al.*, 2005].

[48] The global and annual mean lifetime of contrail segments in CoCiP is 1.9 h, slightly smaller than the delay time derived from the fits. The lifetime of contrails may be smaller in CoCiP than observed because including the many short-lived contrails invisible to MSG. The lifetime may be larger than the delay time when many contrails get advected with the wind out of the corridor and persist outside. On the other hand, persistent contrails enter NAR also when formed upstream in the corridor. For traffic and ECMWF data for 2006, the annual mean residence time of aviation emissions from traffic inside the NAR is about 9.3 ± 7.1 h with large day-to-day variance. The mean (E and N) wind components of (28 ± 14 and $1 \pm 4\,\mathrm{m\,s^{-1}}$) point mainly into easterly direction and imply advection time scales of about 1 day for the NAR. Hence, contrails formed upstream of NAR often get advected into the NAR and later leave with the wind downstream, so that contrails with lifetimes exceeding one day may be included in the NAR observations. From the results of a simulation with traffic restricted to NAR minus the results for total traffic, we diagnose that 18% (27 and 11%) of the contrail cover inside NAR (NAR-W and

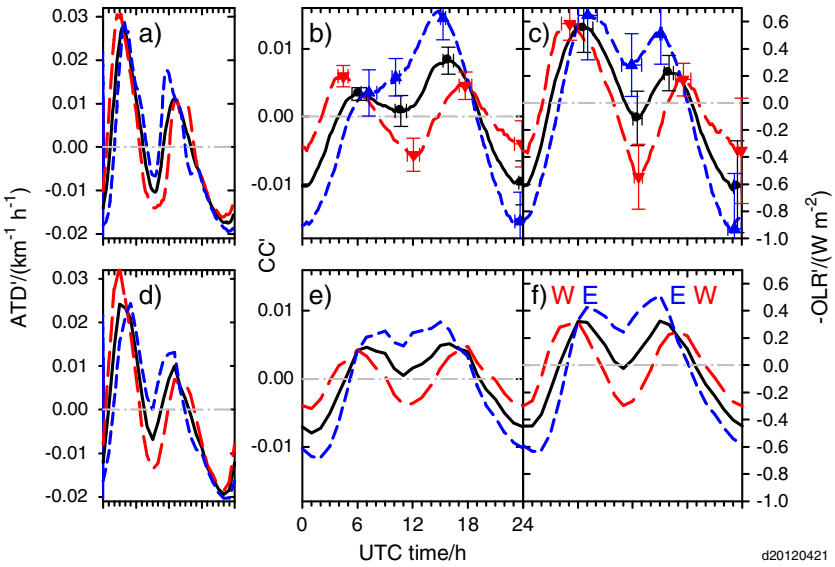

Figure 6. Diurnal cycle differences between NAR and SAR, from observations (top) and model results (bottom). The primed quantities are the deviations from the daily mean values, see equation 2. From left to right: differences in airtraffic density ATD, cirrus cover CC, and OLR. Top: observed EUROCONTROL traffic data and MSG (MeCiDA2/RRUMS) derived cover and OLR data. The error bars indicate the standard deviations based on eight individual annual mean values. Bottom: ACCRI airtraffic data and CoCiP model results.

Table 3. Minima/Maxima Coordinates of Computed and Observed Diurnal Cycle NAR-SAR Difference Deviations. The First and Third Columns List the Times in h, the Second and Fourth Column List Cover in Percentage, and OLR in $W\,m^{-2}$. The Three Blocks Refer to Differences in ATD, CC, and OLR; the First Two Columns are From ACCRI/CoCiP and the Last Two From EUROCONTROL/MSG. Note the Different Time Resolutions: CoCiP Output: 1 h; Observation: 15 min. Standard Deviations are Given for the MSG Data

ACCRI			EUROCONTROL
Time (h)	ATD′ ($h^{-1}\,km^{-1}$)	Time (h)	ATD′ ($h^{-1}\,km^{-1}$)
3	0.0242	3.75	0.0277
9	−0.0068	9.5	−0.0104
13	0.0100	13	0.0110
22	−0.0194	22.75	−0.0175
Modeled		Observed	
Time (h)	CC′ (%)	Time (h)	CC′ (%)
7	0.467	6.03 ± 0.76	0.398 ± 0.25
10	0.150	10.62 ± 0.83	-0.009 ± 0.24
16	0.518	15.63 ± 0.82	0.871 ± 0.26
1	−0.795	24.00 ± 0.72	-1.121 ± 0.16
Modeled		Observed	
Time (h)	LW RF′ ($W\,m^{-2}$)	Time (h)	−OLR′ ($W\,m^{-2}$)
6	0.322	6.69 ± 0.64	0.594 ± 0.33
11	−0.025	11.81 ± 0.34	-0.099 ± 0.18
15	0.323	$1.6.00 \pm 0.65$	0.231 ± 0.23
0	−0.446	23.69 ± 0.76	-0.693 ± 0.27

NAR-E) originates from contrails formed outside NAR. Only about 0.9% of the cover and 0.6% of LW RF over "England" (3°W to −5°E and 50°N to −58°N) results from contrails formed in NAR, according to CoCiP. Hence, most contrails form and decay within a distance of 150–800 km (estimated from the given wind and 3–5 h lifetime), within NAR, so that the lifetime of contrails is not much different from the delay time.

[49] Figure 1 shows also the annual mean LW RF distribution. For single contrail segments, the RF values well exceed $50\,W\,m^{-2}$ locally, as also observed [*Vazquez-Navarro*, 2009]. The regional mean values are far smaller than the maximum values. The model computes mean LW RF values of $3\,W\,m^{-2}$ over mid Europe (10°W–20°E and 40°N–55°N), $1\,W\,m^{-2}$ over continental USA (130°W–65°W and 25°N–55°N), $0.72\,W\,m^{-2}$ in the NAR, and $0.126\,W\,m^{-2}$ globally.

[50] Figure 5 shows the computed results for cover and LW RF in comparison to the fit results as explained in section 3.2. CoCiP simulates the aviation fingerprint with about the same response amplitudes as derived from the observation fits on average, both for cover and RF. The deviation between CoCiP and the mean fit result is smaller than the variability of individual annual results. Still, some diurnal cycle details differ from the fit results. The model computes slower responses in cover and OLR to ATD and smaller differences between the maxima and the noon-minimum than observed.

[51] For NAR, CoCiP computes a mean contrail cirrus contribution to cover of 1.3% and an LW RF of about $720\,mW\,m^{-2}$, which is close to the best estimates of about 1.5% (1–2%) cover and $750\,mW\,m^{-2}$ ($600–900\,mW\,m^{-2}$) derived from the observations and the linear response model fits. The computed cover would increase when reducing the optical depth threshold for cirrus (here 0.1). Contrail CC increases by a factor of 1.78 in NAR when the threshold is reduced by a factor of 5 (0.02 instead of 0.1). Globally, this factor is 1.91. The comparison suggests that the optical depth threshold for contrail cirrus detection by MeCiDA2 may be close to 0.1.

Table 4. Regional (NAR) and Global (G) Longwave (LW), Shortwave (SW), and Net RF Values From Models and Model-based Global Extrapolation of the Observed LW RF (NAR) of 600–$900\,mW\,m^{-2}$

Parameter	CoCiP	ECHAM LiCC	ECHAM CCmod
Model results ($mW\,m^{-2}$)			
RF LW (NAR)	720	41.1	201
RF LW (G)	126	7.9	47
−RF SW (G)	76.8	2	9
RF net (G)	49.2	5.9	31
Ratios			
RF LW NAR/RF LW G	5.71	5.20	4.28
RF LW NAR/RF net G	14.6	6.97	6.48
−RF SW G/RF LW G	0.609	0.253	0.191
Extrapolation ($mW\,m^{-2}$)			
RF LW (G)	105–158	115–173	140–210
RF net (G)	41–62	86–129	93–139
RF net (G) for −SW/LW = 0.4	63–95	69–104	84–126

[52] The observations and the CoCiP results show the same diurnal double wave with all its W-E fingerprint characteristics. The double wave and its W-E variability are best visible in deviations from daily mean values, CC′ and RF′ (or −OLR′) in NAR and its W and E parts, see Figure 6. Table 3 lists the coordinates of the extreme value points for NAR-SAR. The traffic data from ACCRI and those from EUROCONTROL agree within 10% in amplitudes and better than 1 h in time. Parts of the differences are due to ATD time uncertainties which led us to shift the ACCRI traffic by 1 h forward compared to what has been reported in the ACCRI data. The modeled and observed maximum OLR values differ by 35–45%. However, the modeled and observed diurnal cycle results are reasonably well correlated (ρ larger than 0.9). The results show that the observations and response model results are reasonably consistent with a physical contrail cirrus model.

3.4. Extrapolation of Regional Results to Global Results

[53] Global extrapolation requires models to compute the "extrapolation ratio" between the unknown global RF values (LW and net) and the regional observation-derived LW RF in the NAR. In principle, the extrapolation ratio is sensitive to the contrail formation potential in NAR relative to the globe and to the traffic distribution (for example relative to the tropopause).

[54] Therefore, we use two further models in addition to CoCiP for extrapolation, see Table 4. The table includes data provided by C. Frömming and U. Burkhardt (personal communication, 2012) based on published simulation results from ECHAM LiCC, a linear contrail model with meteorology from the global climate model ECHAM4 [*Frömming et al.*, 2011], and from ECHAM CCmod, a global climate model simulating the life cycle of contrail cirrus as part of a cirrus model within ECHAM4 [*Burkhardt and Kärcher*, 2011]. For RF from ECHAM CCmod, we include the published net RF result with feedback of water uptake by contrails on cirrus, while the regional LW RF values are available only without feedback.

[55] The global estimates are obtained by dividing the regional results by the extrapolation ratio.

[56] The contrail cover ratios are less important for RF estimates. Still, the three models predict a surprisingly small range of NAR/global cover ratios: 4.34–5.56 (with CoCiP at the high end). This ratio depends nonlinearly on the threshold optical depth values used for cover definitions.

[57] As explained above, the observations and response model fits imply an AIC contribution to OLR or LW RF of 0.6–0.9 W m^{-2}. In the three models, the RF LW NAR is 6.5–14.6 times larger than the global net RF. Hence, we obtain global estimates of the net RF of 41–139 mW m^{-2}.

[58] Part of this large range is caused by different shortwave (SW)/LW RF ratios (in terms of SW magnitude) between 0.19 and 0.61. As discussed in Appendix B, the SW/LW ratio is sensitive to many parameters. When recomputing the net RF for an assumed SW/LW ratio of 0.4, the net RF globally scatters in a smaller range of 63–95 mW m^{-2}.

[59] Hence, the extrapolation of the observation-derived RF LW in NAR to the global mean net AIC RF based on CoCiP provides a best estimate of about 50 mW m^{-2} (40–80 mW m^{-2}). The magnitude of this value is slightly towards the upper end of earlier results [*Minnis et al.*, 2004; *Stordal et al.*, 2005; *Sausen et al.*, 2005; *Lee et al.*, 2009; *Burkhardt and Kärcher*, 2011]. Net RF values exceeding 100 mW m^{-2} could not be excluded if the SW/LW RF ratio would be as small as computed in previous studies.

4. Discussion

4.1. South-North Differences and Nonaviation Background Estimates

[60] If the mean cirrus and OLR signals without aviation impact would be fully symmetrical between NAR and SAR, any difference between NAR and SAR statistics would be purely caused by aviation. Because of geographic symmetry and similar ocean conditions, some similarity between the NAR and SAR climatologies can be expected. However, the South Atlantic climatology differs from that in the North Atlantic for many reasons, including different continent, ocean, air composition, and aerosol distributions in the two regions. They are reflected, e.g., in different cirrus mean values (Figure 2). They also show up in annual mean tropopause temperature differences [*Wilcox et al.*, 2012]. The sea surface temperature cycles differ between NAR and SAR by about 10–30% of the regional values [*Kennedy et al.*, 2007]. For comparison, the amplitudes of the diurnal cycle of SEVIRI brightness temperatures for SAR vary between 0.5 and 1.2 K depending on channel wavelength in our data analysis. A surface temperature amplitude of 0.1 K implies typically about 0.15 W m^{-2} amplitude at top of atmosphere based on libRadtran data [*Mayer and Kylling*, 2005]. Tests with other background assumptions (e.g., constant background and or Fourier series with adjustable amplitudes) and other response functions [*Graf et al.*, 2012] show that the aviation fingerprint shows up also in these alternatives, but the range of derived RF values is about a factor of two larger than estimated with SAR background.

[61] The SOT model explains about 75% of the seasonal variance of the diurnal cycle of OLR in SAR (Appendix A). The deviations of observed OLR from the solar tide model

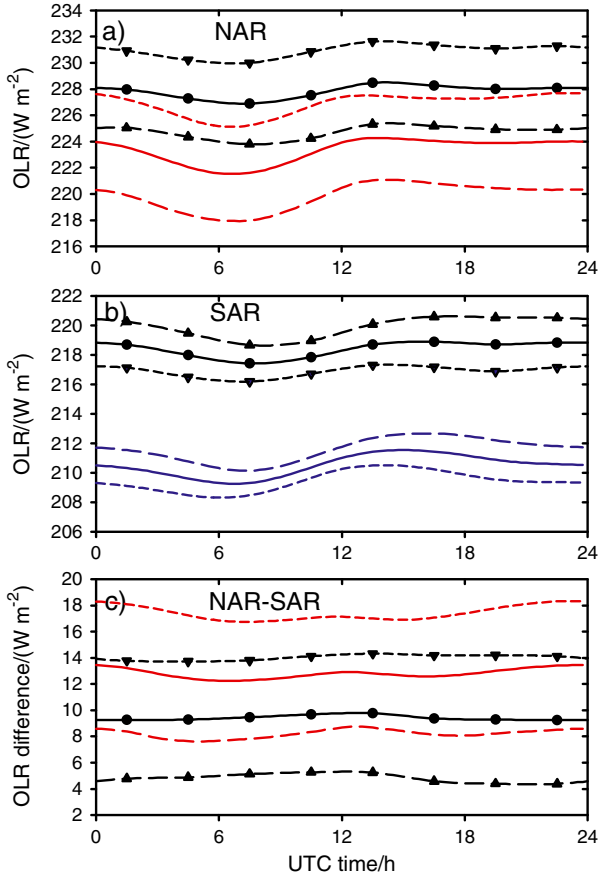

Figure 7. Mean diurnal cycles of OLR from ECMWF average over the last 2 days of the two 6-day forecasts for 2011 (symbols according to the 3-h time resolution of the data, spline interpolated black curves) and from Meteosat-RRUMS OLR (8-year mean, colored curves) for (a) NAR, (b) SAR, and (c) NAR-SAR difference, in the total region (full curves) and for the western (long dashed) and eastern parts (short dashed).

are larger on NAR than on SAR, which indicates a larger anthropogenic influence on NAR.

[62] The background atmosphere without aviation effects, as needed for this study, may be derived from global circulation weather and climate models. Numerical weather predictions experience aviation effects in the initial conditions, and their diurnal cycle gets disturbed by the data assimilation process. However, the initial disturbances decay after a few days of forecast time. Similar to CC results shown in *Graf et al.* [2012], we computed, therefore, the mean OLR cycles for OLR data available from ECMWF medium-range forecasts with 3-h time resolution for the year 2011. The variance is reduced by averaging over four diurnal cycles from the last 2 days of two 6-day forecasts, starting at 0 and 12 UTC each day. The mean ECMWF cycle results are compared with the mean MSG-RRUMS derived OLR data in Figure 7. From similar results for the years 2007–2011, the standard deviations of the diurnal cycle amplitudes are computed to be less than 0.1% for cover and 0.1 W m^{-2} for RF in NAR, and 60% smaller in SAR. The differences of regional mean values (5–8 W m^{-2}, less than 4%) are in line with other comparisons (Appendix C) but unimportant for this discussion. One cannot expect a perfect agreement between such a model and

observations. In fact, the diurnal cycles derived from the two sources show some quantitative differences, but are very similar in shape, phases, amplitudes, and E-W differences, and are consistent with migrating solar tidal waves in SAR and, for ECMWF, also in NAR. The variance of mean values of subsamples (e.g., every fourth or 91st day) of cycles of the differences between NAR and half-year shifted SAR results is at least 0.2 $W m^{-2}$. The mean OLR cycle differences of the ECMWF data between NAR and SAR show waves with amplitudes below $\pm 0.25 W m^{-2}$, without coherent patterns, which are not significantly different from zero. In contrast, the MSG-RRUMS OLR aviation fingerprint is significant, as shown before. This supports the assumption of SAR providing useful estimates for NAR without aviation.

4.2. Accuracy of the Satellite-derived Cover and Outgoing Longwave Radiation

[63] The accuracy of the CC and OLR values derived from MSG is important for this study. Appendix C compares the MSG results with data from the ECMWF [*Morcrette et al*., 2008] and from other satellite observations. The RF results depend on the OLR data derived from MSG-SEVIRI with RRUMS [*Vazquez-Navarro et al*., 2012]. We find that RRUMS agrees within about 2% for regional mean OLR with data from three sources: ECMWF, ERBE [*Smith and Rutan*, 2003; *Smith et al*., 2008], and GERB [*Harries et al*., 2005; *Comer et al*., 2007] and shows similar standard deviations. The accuracy of the mean values is less important than those of diurnal variations. Monthly mean OLR diurnal cycle data derived from GERB and CERES data by the EUMETSAT Satellite Application Facility on Climate Monitoring (CM-SAF) [*Schulz et al*., 2009] support the fingerprint results derived with RRUMS. Hence, the accuracy of the cover and OLR observations does not limit the accuracy of the RF values derived.

4.3. Consistency of Cover Change and Radiative Forcing

[64] Can about 1.5% additional contrail CC explain $0.8 \pm 0.3 W m^{-2}$ of LW RF (see section 3.2)? Here, we provide an order of magnitude argument. The LW RF from a globally homogeneous cirrus layer at 10.5 km altitude in a cloudy atmosphere with 1% cover and optical depth of 0.3 amounts to about 0.3 $W m^{-2}$ (0.2–0.34 $W m^{-2}$) [*Myhre et al*., 2009]. CoCiP computes a mean optical depth of contrail cirrus of about 0.2. For a linear RF-cover-depth relationship, an LW RF of 0.3 $W m^{-2}$ is to be expected for 1.5% cover of optical depth 0.2 in the NAR. This does not suffice to explain the observations. The remaining 0.5 $W m^{-2}$ (0.3–0.6 $W m^{-2}$) may come from aircraft emissions and contrails forming additional light-scattering particles inside cirrus and hence making them optically thicker without adding further cover. An increase of optical depth by, say, 0.2 in a cirrus with typical optical depth values of 0.5 would increase LW RF by about 0.1 $W m^{-2}$ for 1% CC [*Markowicz and Witek*, 2011]. Hence, if contrails increase the optical depth by 0.2 in 5% preexisting CC, then this could explain the missing 0.5 $W m^{-2}$. Persistent contrails may form inside optically thin cirrus since ice supersaturation in cirrus has been observed [*Jensen et al*., 2001; *Ovarlez et al*., 2002; *Stubenrauch and Schumann*, 2005; *Immler et al*., 2008; *Iwabuchi et al*., 2012]. Hence, the large observed OLR/cover ratio may be explained with aviation not only inducing additional CC but also making existing cirrus optically thicker. Further evidence becoming available now from contrail and cirrus observations with MODIS (Patrick Minnis, paper submitted and presented at the ACCRI Symposium, Virginia Beach, USA, November 2012) and from observations of the diurnal cycle of the optical depth of cirrus in NAR and SAR derived from Meteosat and CALIPSO data [*Kox*, 2012] should be used to further test the suggested explanation and, if possible, to constrain the contributions from contrails and possibly other aviation effects to the observed cirrus changes.

5. Conclusions

[65] This paper provides methods and observations to constrain the RF from aviation-induced cloud changes at diurnal time scales. The methods employ an aviation fingerprint in traffic data, a diurnal double wave with large systematic diurnal variability and characteristic east-west differences, that has been recently identified also in satellite-observed cloud cover over the North Atlantic [*Graf et al*., 2012]. The method detects contrail cirrus without reference to line structures. Here, this approach is extended to study net outgoing LW radiances at top of the atmosphere and to estimate regional and global RF with models from the derived change in OLR.

[66] The method has been applied to 8 years of Meteosat CC and OLR data derived for a NAR and a SAR with previously developed methods from Meteosat SEVIRI infrared data. The data show diurnal cycles results supported by other satellite and ECMWF weather forecast data. The agreement between such data is better for OLR than for CC, partially because OLR is better defined.

[67] In spite of strong day-to-day variability, the aviation fingerprint shows up also in annual results, in particular as double wave with west-east differences in correspondence to the special traffic cycle and in north-south differences of CC and OLR (NAR-SAR, regions with and without airtraffic). The diurnal cycles show statistically significant patterns in the 8-year mean. The aviation fingerprint is found also in the 8-year monthly and seasonal mean diurnal cycles. As for cirrus, the OLR fingerprint pattern is the strongest with the shortest delay times in summer and autumn.

[68] The amplitude and the time scales of the response are derived by fitting the mean diurnal cycle results to airtraffic data (here for 2004) with linear response models. The results depend on the response functions used [*Graf et al*., 2012] and on the assumed background cycle for an atmosphere without aviation. The present study estimates the background cycle from observations in the South Atlantic.

[69] The observed diurnal cycles of cover and OLR show a double wave also in the South Atlantic. However, the double wave in SAR migrates with the sun, without the aviation fingerprint in west-east differences. As for CC [*Graf et al*., 2012], this is supported by ECMWF data. The natural diurnal OLR cycle may be caused by different daytime warming and nighttime cooling of the atmosphere by radiation. A solar tide model, which relates OLR to temperature tide results in the troposphere, explains a large fraction of the diurnal and seasonal variability in the South Atlantic. In the North Atlantic, the OLR signal deviates significantly

from the solar tide pattern. This provides a traffic data-independent argument for aviation effects in NAR.

[70] In principle, the climatology in the SAR differs from a hypothetical NAR without aviation for many reasons. The similarity of the diurnal cycles of CC and OLR in SAR and NAR without aviation is supported by ECMWF medium-range weather forecast data. The aviation fingerprint is most obvious in west-east differences of the NAR-SAR difference. Fits with the observed NAR-SAR difference considerably improve the OLR fits compared to an assumed constant background. The fits improve further when including the solar tide correction for NAR-SAR differences.

[71] For NAR, the data analysis suggests a cover of 1–2% aviation-induced additional cirrus with optical depth larger than about 0.1, LW RF of 600–900 $\mathrm{mW\,m^{-2}}$, and mean delay times of 3–4 h. The detected linear contrails contribute a small fraction to the contrail CC and exhibit smaller time scales. The regional RF estimate includes all aviation-induced radiation changes effective at diurnal time scales. The contrail cirrus model (CoCiP) shows a similar aviation fingerprint as the observations. Hence, contrail cirrus may be mainly responsible for the observed effects at diurnal time scales. The large RF to cover ratio suggests that aviation does not only induce additional CC but also makes existing cirrus optically thicker. This suggestions should be tested with further data that are becoming available, e.g., on the diurnal cycle of the optical depth of cirrus.

[72] Global extrapolation uses the ratio between regional and global aviation contributions as derived with CoCiP and with two further models. The OLR change deduced for the North Atlantic implies a global LW RF from AIC at diurnal scales of about 100–160 $\mathrm{mW\,m^{-2}}$. The extrapolation is sensitive to the distributions of airtraffic and humidity, but the three global contrail models show similar ratios for LW RF in spite of different meteorological data and fundamentally different model approaches. Still, this extrapolation might change when further evidences become available.

[73] The global net RF depends strongly on the degree of cancelation of positive LW RF by the negative SW RF. Previous studies report highly different ratios of the SW and LW RF magnitudes, which depend on many particle, atmosphere, surface, and traffic details. Extrapolation based on CoCiP results (for traffic and weather input data for 2006) suggests a net RF from AIC of about 50 $\mathrm{mW\,m^{-2}}$ (40–80 $\mathrm{mW\,m^{-2}}$). If the SW/LW ratio is 0.4 instead of 0.6, the net RF would be 50% larger. The results may change when improved models and further observations become available. In particular, the uncertain SW/LW ratio needs further research.

[74] This study would not be possible without temporally and spatially resolved airtraffic data. The existing data cover only part of the 8-year period and have uncertain accuracy over the oceans. Further and possibly improved data would allow studying the traffic variability over the years and the effects of systematic correlations between traffic and cirrus for certain weather patterns.

[75] The present method takes advantage of a special diurnal airtraffic cycle. Similar cycles are to be expected along other long-distance routes, such as over the North Pacific and Siberia, and over parts of the USA. In a future study, one may consider patterns with combined temporal and spatial variability, e.g., over mid Europe. Further research may refine the present estimates of aviation-induced cloud and radiation changes.

Appendix A

Solar Tide Influence on the Regional Differences of Longwave Radiation

[76] We construct an OLR solar tide model (SOT) based on solar tide temperature data to approximate the diurnal OLR NAR-SAR tide differences with high time resolution. Diurnal and semidiurnal atmosphere temperature tide results for NAR and SAR are available from the GSWM, a steady state noise-free numerical global atmospheric solar tide model [*Hagan and Forbes*, 2002, 2003], The temperature results are available for each month from http://www.hao.ucar.edu/modeling/gswm/gswm.html. The SOT model assumes that the OLR′ tides are directly proportional to the atmospheric solar tide temperatures in the lowest 4-km layer of the GSWM model. This simplification is justified by the high correlation between the model result and observed OLR′ in SAR ($\rho = 75\%$). The temperature in the lowest layer provides the highest correlation coefficient between the SOT model and observed OLR′ values in SAR. Temperature dominates water vapor contributions to OLR in the lower and middle troposphere [*Huang et al.*, 2007]. The temperature tides are scaled with one single factor minimizing the sum of the squared deviations from monthly mean OLR′ in SAR over 8 years. The same value is applied then also for NAR.

[77] Figure A1 shows the OLR tide model results and the observed OLR results for NAR and SAR. On NAR, each morning, we see systematic undershooting of the observed OLR below the model result, and we see afternoon OLR minima for most months. On SAR, such undershooting and afternoon minima occur only rarely and with lower

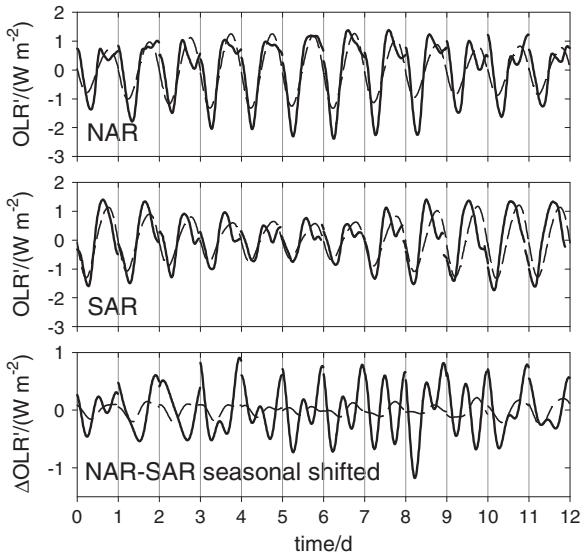

Figure A1. Eight-year mean of monthly mean diurnal cycles of OLR′ deviations as derived with RRUMS (thick full) compared to a solar tide model of OLR′ (thin dashed) on NAR (top) and SAR (middle). The lowest panel shows the NAR-SAR difference with seasonal shift of SAR results by 6 months. Each panel shows 12 monthly mean diurnal cycle results versus time of day, shifted by 1 day for each month from left to right, from January to December.

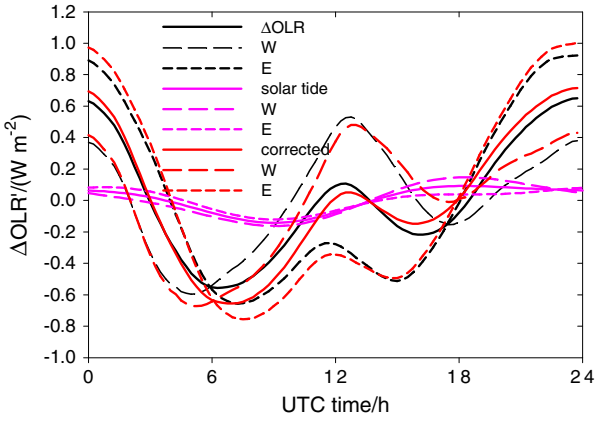

Figure A2. OLR annual mean cycle difference between NAR and SAR after subtraction of diurnal mean values. Black: RRUMS observations; red: solar tide model (SOT); pink: observed minus the solar tide difference. Full curve: total region; long dashed: west; short dashed: east part.

amplitude. The RMS deviations between observed and modeled OLR values are $0.532 \pm 0.085\,\mathrm{W\,m^{-2}}$ on NAR and $0.344 \pm 0.035\,\mathrm{W\,m^{-2}}$ on SAR in the annual mean. The model explains 0.771 ± 0.045 of the variance on SAR but 0.673 ± 0.070 on NAR, hence, significantly more on SAR than NAR in the 8-year average.

[78] Figure A1 also shows the OLR difference between NAR and SAR with a 6-month shift (from the NAR OLR signal in January, we subtract the SAR OLR signal in July, etc.). The variance of the NAR-SAR differences in the observed OLR values is large: it amounts to 31% of the OLR-SAR variance. In contrast, the NAR-SAR difference in the SOT cycle is small, less than 2% of the OLR-SAR variance. Hence, the observed NAR-SAR OLR difference cannot be explained by the solar tide. The observed NAR-SAR OLR difference exhibits the aviation fingerprint for most months, with February and March as exceptions, when most airtraffic occurs above the tropopause. Hence, the monthly results support the fingerprint identified from annual mean values for most of the year.

Table A1. Longwave (LW), Shortwave (SW), and Net Radiative Forcing in $\mathrm{W\,m^{-2}}$ for an Idealized Case With 1% Homogeneous Cirrus Cover. Abbreviations: UiO-BBM, University of Oslo-broadband model; UoR-FU, University of Reading-Fu and Liou model; UW-FU, University of Warsaw-Fu and Liou model; UoL-E-S, University of Leads-Edwards-Slingo radiation code; CNRM-ARPEGE, Centre National de Recherches Meteorologiques-Action de Recherche Petite Echelle et Grande Echelle

Reference	LW	−SW	Net	−SW/LW
Myhre and Stordal [2001]	0.21	0.09	0.12	0.43
Stuber and Forster [2007]	0.19	0.06	0.13	0.32
Myhre et al. [2009]				
UiO-BBM UiO-BBM	0.202	0.105	0.097	0.52
UoR-FU	0.203	0.079	0.124	0.39
UW-FU	0.229	0.082	0.148	0.36
UoL-E-S	0.276	0.119	0.158	0.43
CNRM-ARPEGE	0.34	0.15	0.19	0.44
Rap et al. [2010]	0.22	0.1	0.12	0.45
Frömming et al. [2011]	0.21	0.07	0.14	0.33
Markowicz and Witek [2011]	0.200	0.070	0.130	0.35
Schumann et al. [2012]	0.213	0.117	0.096	0.55

Table A2. Radiative Forcing in $\mathrm{mW\,m^{-2}}$ for Contrails in Global Simulations. The Optical Depth τ_s at 550 nm is Listed When Fixed in the Simulations; Otherwise, Variable τ_s is Computed in the Model. The Column "d.c." Identifies Whether the Diurnal Traffic Cycle is Included. The Table Lists All-sky Results, Unless Noted Otherwise

Reference	τ_s	d.c.	LW	−SW	Net	−SW/LW
Minnis et al. [1999]	0.3	yes	25	8	17	0.32
Myhre and Stordal [2001]	0.3	no	20	9	11	0.45
	0.3	yes	20	11	9	0.55
Marquart et al. [2003]		no	4.9	1.4	3.5	0.29
Stuber and Forster [2007]	0.1	yes	3.34	1.35	1.99	0.40
Clear sky	0.1	yes	4.54	2.39	2.14	0.53
Rädel and Shine, 2008	0.1	yes	13.6	7.2	6.4	0.53
Rap et al. [2010] Offline	≈0.2	yes	21	9	12	0.43
Online	0.1	yes	6.3	2.4	3.9	0.38
Online	0.2	yes	11.5	3.8	7.7	0.33
Online	0.3	yes	17.1	5.5	11.6	0.32
Frömming et al. [2011]		no	7.9	2	5.9	0.25
		yes	7.3	2.4	4.9	0.33
Burkhardt and Kärcher [2011]		yes	47.1	9.8	37.3	0.21
Markowicz and Witek [2011]	0.3	no	20.9	9.9	11	0.47
This paper, CoCiP		yes	126.1	76.8	49.2	0.61

Table A3. Annual Mean Values of Cirrus Cover and OLR with Standard Deviations in NAR and SAR. The Last Three Blocks List the Annual Mean Solar Direct Radiation (SDR), the Reflected Solar Radiation (RSR), and the Effective Albedo RSR/SDR for NAR

Cirrus cover	MeCiDA2	ECMWF	Zonal means	
NAR	0.285 ± 0.129	0.333 ± 0.152	0.29–0.51	
SAR	0.330 ± 0.172	0.337 ± 0.175	0.26–0.39	
OLR ($W\,m^{-2}$)	RRUMS	ECMWF	ERBE	CM-SAF
NAR	223.9 ± 16.3	228.3 ± 14.9	219.5 ± 13	227.7 ± 11.9
SAR	211.3 ± 14.3	221.1 ± 13.1	212.8 ± 6	209.9 ± 9.1
SDR ($W\,m^{-2}$)	RRUMS	ECMWF		
NAR	284.6	284.6		
RSR ($W\,m^{-2}$)	RRUMS	ECMWF		
NAR	112.2	99.8		
Albedo	RRUMS	ECMWF		
NAR	0.394	0.351		

[79] The annual mean NAR-SAR differences $C_{SOT}(t_i)$ for the total regions and its W and E parts are shown in Figure A2. The signal contains a diurnal and a semidiurnal mode. The maximum amplitude is about $0.15\,W\,m^{-2}$, far smaller than the observed OLR amplitude. The annual mean NAR-SAR difference from this model, $C_{SOT}(t_i)$ for OLR, is used to correct the background part of the response model for climatological differences between OLR in NAR and SAR in the fit method of section 2.6.

Appendix B

The Ratio of Shortwave/Longwave Radiative Forcing

[80] The SW, LW, and net RF from thin cirrus and contrails have been computed in several studies. Table A1 lists results of a homogeneous cirrus test case [*Myhre et al*., 2009] and Table A2 those of global contrail studies. Studies including the diurnal airtraffic cycle show about 20–30% larger SW/LW ratios than for constant traffic. Published mean SW/LW magnitude ratios vary between 0.21 and 0.55, while CoCiP computes a relatively large SW/LW ratio of 0.6 globally.

[81] Contrail RF derived for many case studies from Meteosat SEVIRI data shows larger SW/LW ratio of 0.91 over ocean and 0.82 over land on average over 845 individual day and night contrails [*Vazquez-Navarro*, 2009; *Vazquez-Navarro et al*., 2010]. For a single day with a long lasting contrail cirrus, a SW/LW ratio close to one was derived using Meteosat GERB data [*Haywood et al*., 2009].

[82] RF increases nonlinearly with the optical depth τ_s of the contrails [*Fu et al*., 2000]. This may cause a larger SW/LW magnitude when the RF is computed for an ensemble of cirrus cases with different optical depth values as in

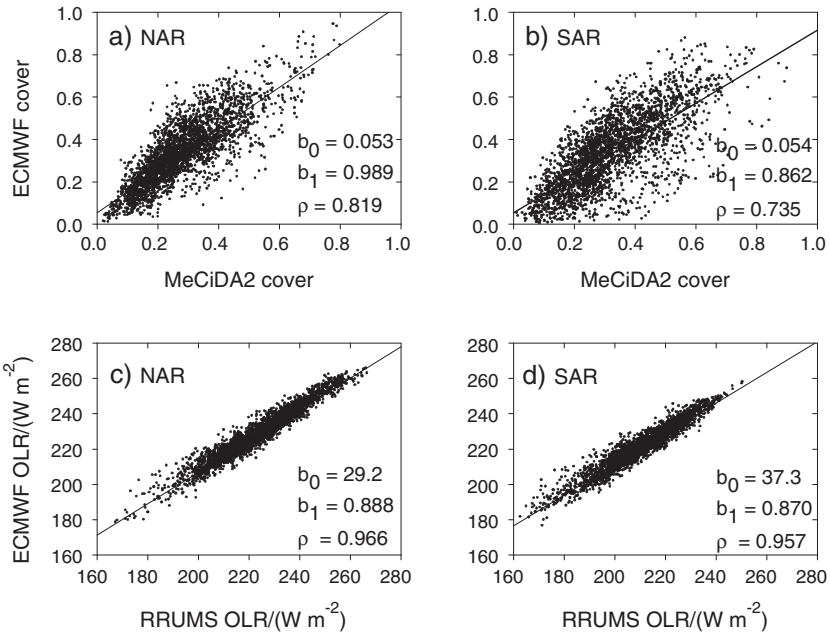

Figure B1. Scatter plots of ECMWF forecast values versus MSG-derived (MeCiDA2 or RRUMS) observations for the year 2006. Each dot represents a regional mean value in NAR or SAR every 3 h. Top: cirrus cover; bottom: OLR. Left: NAR; right: SAR. Bias b_0, slope b_1, and correlation coefficients ρ for linear regressions are as listed.

CoCiP than for the mean values. The result also depends on the treatment of cloud overlap between contrails and other clouds. In addition, the SW/LW ratio depends on particle shape and size, on the correlation of contrail occurrence with solar zenith angle, and on the difference between the temperature in the contrails and Earth-atmosphere brightness temperature [*Markowicz and Witek*, 2011; *Schumann et al*., 2012]. The SW/LW RF ratio further depends on the radiation budget of the Earth globally and regionally. From the ECMWF data for 2006, we find global mean values of OLR of 245 W m^{-2}, reflected SW radiation of 100 W m^{-2}, incoming radiation of 344 W m^{-2}, and planetary albedo of 0.29. These values agree within a few percent with multiannual best estimates [*Trenberth et al*., 2009; *Loeb et al*., 2009]. OLR is lower and albedo is higher in NAR than globally, see Table A3. A higher Earth-atmosphere albedo may reduce the SW/LW ratio [*Meerkötter et al*., 1999].

Appendix C

Comparison of Meteosat-derived Data With Other Data

[83] Three-hourly mean cover values of MeCiDA2 and OLR values from RRUMS are compared with CC (with optical depth >0.1) and OLR values derived from ECMWF input for NAR and SAR in the year 2006, see Figure B1. The agreement is better for OLR than for CC but far from perfect. The deviations are far larger than those expected from aviation contributions. The forecasts give better agreement on NAR than on SAR, presumably because of more observational data input included in the forecast.

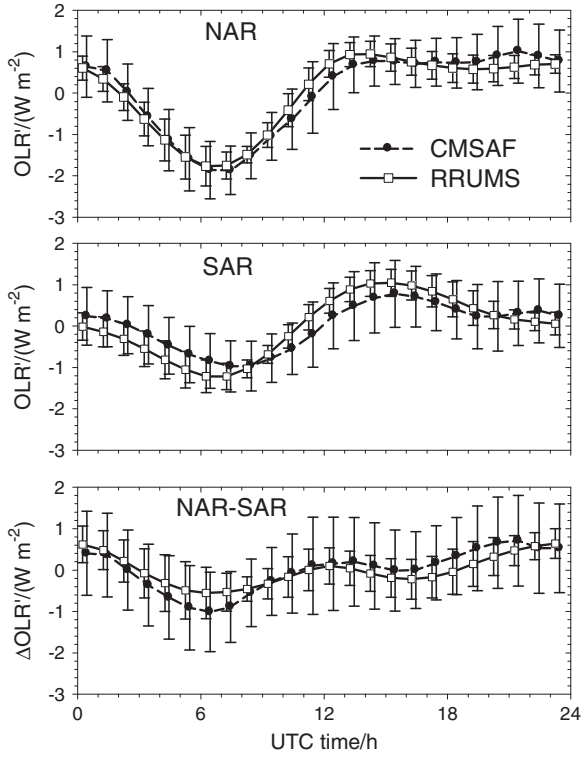

Figure C1. Comparison of OLR′ from RRUMS (open squares, full line) and CM-SAF (dots, dashed line), showing the multimonth mean diurnal cycle of OLR deviations from daily mean values. The error bars indicate the standard deviations of the monthly mean values (96 for RRUMS, 39 selected for CM-SAF) at the given day time.

[84] Satellite-observed annual mean CC and computations show large differences, see Table A3. MeCiDA2 and ECMWF regional mean CC values differ by nearly 30%. *Stubenrauch et al*. [2010] report zonal mean high cloud cover results from various satellites and data analysis: The annual mean values for 30°–60°N and 30°–60°S are reported in Table A3. High cloud cover, just as temperature and tropopause altitude [*Wilcox et al*., 2012], varies considerably with longitude, so that zonal mean values are not directly comparable to our regional results. Differences may also be caused by different cloud cover definitions. For OLR, Table A3 compares mean results from RRUMS with data from three sources, as explained below. We find that RRUMS agrees within about 2% with the three data sets in terms of the mean OLR values and shows similar standard deviations.

[85] The diurnal cycles of CC [*Bergman and Salby*, 1996; *Wylie*, 2008; *Stubenrauch et al*., 2006] and of OLR [*Comer et al*., 2007; *Smith and Rutan*, 2003; *Smith et al*., 2008] have been investigated in previous studies, but only a few results are available for quantitative comparison in NAR and SAR.

[86] *Smith et al*. [2008] derived the diurnal cycle of OLR from 5 years of ERBE measurements. From the data (D. Rutan, personal communication, 2008), we computed the diurnal cycle of OLR for NAR and SAR. RRUMS finds daily OLR amplitudes of 2.8 W m^{-2} for NAR and 2.3 W m^{-2} for SAR, where the ERBE data imply larger OLR amplitudes of 9.9 and 6.6 W m^{-2}, respectively. Such differences may be caused by seasonal changes and the 72 day precession time of the satellite orbit, particular near the latitude extremes of the orbit [*Smith and Rutan*, 2003]. This was confirmed by tests with simulated ERBE data for fictive orbits of an ERBE in 2004–2012 (provided by L. Nguyen and P. Minnis, 2012) and Meteosat-RRUMS derived OLR estimates.

[87] Compared to ERBE, significantly smaller amplitudes of the OLR diurnal cycle were found in GERB data [*Comer et al*., 2007]. The diurnal OLR amplitudes are 5 W m^{-2} over the tropical South Atlantic (10°–20°S and 0°–10°W). The diurnal and semidiurnal contributions in the 1-month mean values are noisy but smaller in general over the Atlantic Ocean than over land and smaller at high latitudes than in the tropics. This supports the magnitude of the RRUMS OLR amplitude results.

[88] For test of the OLR values derived with the RRUMS method, we compared with monthly mean diurnal cycles of OLR, called TETmd, from the CM-SAF. The data were downloaded (in May 2012) and used to compute the mean values for NAR and SAR for all months from February 2004 to January 2012. Note that the CM-SAF data use GERB and GERB-like SEVIRI data for visibility zenith angles (VZAs) below 70° and data from CERES on Aqua/Terra for VZA $>80°$ and use a linear interpolation between both in the VZA transition range. The NAR/SAR regions spread over VZA range from 53°–76°. Hence, the CM-SAF and RRUMS data, though partially derived from the same satellite,

represent essentially independent observations. The mean values over all 96 monthly records are listed in Table A3. The CM-SAF results are less than 0.3% or about 0.62 W m^{-2} (0.53 W m^{-2}) smaller than RRUMS on NAR (SAR), which is a small deviation.

[89] CM-SAF provides monthly mean diurnal cycles with 1 h time resolution. We found that several of the monthly cycle results exhibit deviations from a harmonic signal because of data gaps (confirmed by N. Clerbaux, personal communication, 2012). Therefore, we selected those in which OLR values at successive hourly times (assuming a periodic signal) differed not more than 1 W m^{-2}. This filter selected 39 monthly records out of 96. Similarly, monthly mean diurnal OLR cycles were computed from RRUMS (96 months, excluding malfunction flagged data). The results are plotted in Figure C1. We see good agreement between CM-SAF and RRUMS within the respective standard deviations. Both data sets show the fingerprint signature, in particular in the NAR-SAR difference. We also considered NAR-W and NAR-E cycles from CM-SAF and found them consistent with the expected temporal shifts of the fingerprint.

[90] **Acknowledgments.** This work contributed to the Deutsches Zentrum für Luft- und Raumfahrt (DLR) project "Climate-compatible Air Transport System," the project "UFO" funded by the German Federal Ministry BMBF, the European project "Reducing Emissions from Aviation by Changing Trajectories for the benefit of Climate," and the FAA ACCRI. ECMWF data were provided within an ECMWF special project. Meteosat 8/9 data were provided by EUMETSAT via the German Remote Sensing data center at DLR, and 2004 airtraffic data were provided by EUROCONTROL, both within the ESA-DUE project "contrails." The 2006 waypoint data were setup by the US Department of Transport Volpe Center using data provided by the US FAA and EUROCONTROL in support of the objectives of the International Civil Aviation Organization Committee on Aviation Environmental Protection CO_2 Task Group. We thank the partner institutions of the IAGOS Research Infrastructure and the participating airlines for providing instrumented airliner flight routes from MOZAIC. We thank the reviewers for critical remarks which helped to improve the paper and many colleagues for support and discussions which contributed to this study.

References

Atlas, D., Z. Wang, and D. P. Duda (2006), Contrails to cirrus – Morphology, microphysics, and radiative properties, *J. Appl. Meteor. Climatol.*, *45*, 5–19, doi:10.1175/JAM2325.1.

Bakan, S., M. Betancor, V. Gayler, and H. Grassl (1994), Contrail frequency over Europe from NOAA satellite images, *Ann. Geophysicae*, *12*, 962–968, doi:10.1007/s00585-994-0962-y.

Bergman, J. W., and M. L. Salby (1996), Diurnal variations of cloud cover and their relationship to climatological conditions, *J. Climate*, *9*, 2802–2820.

Boucher, O. (1999), Air traffic may increase cirrus cloudiness, *Nature*, *397*, 30–31, doi:10.1038/16169.

Brasseur, G. P., and M. Gupta (2010), Impact of aviation on climate – Research priorities, *Bull. Amer. Meteor. Soc.*, *91*, 461–463, doi:10.1175/2009BAMS2850.1.

Bugliaro, L., H. Mannstein, and S. Kox (2012), Ice clouds properties from space, in Atmospheric Physics – Background, Methods, Trends, edited by U. Schumann, Springer, Heidelberg, doi:10.1007/978-3-642-30183-4.

Burkhardt, U., and B. Kärcher (2011), Global radiative forcing from contrail cirrus, *Nature Clim. Change*, *1*, 54–58, doi:10.1038/NCLIMATE1068.

Comer, R. E., A. Slingo, and R. P. Allan (2007), Observations of the diurnal cycle of outgoing longwave radiation from the Geostationary Earth Radiation Budget instrument, *Geophys. Res. Lett.*, *34*, L02823, doi:10.1029/2006GL028229.

Dee, D. P., et al. (2011), The ERA-Interim reanalysis: Configuration and performance of the data assimilation system, *Quart. J. Roy. Meteor. Soc.*, *137*, 553–597, doi:10.1002/qj.828.

Duda, D., P. Minnis, and L. Nguyen (2001), Estimates of cloud radiative forcing in contrail clusters using GOES imagery, *J. Geophys. Res.*, *106*, 4927–4937, doi:10.1029/2000JD900393.

Ewald, F., L. Bugliaro, H. Mannstein, and B. Mayer (2012), An improved cirrus detection algorithm MeCiDA2 for SEVIRI and its validation with MODIS, *Atmos. Meas. Tech. Discuss.*, *5*, 5271-5311, doi:10.5194/amtd-5-5271-2012.

Fahey, D., et al. (1999), Aviation-produced aerosols and cloudiness, in Aviation and the Global Atmosphere. A Special Report of IPCC Working Groups I and III, edited by J. E. Penner, D. H. Lister, et al., pp. 65–120, Cambridge University Press, New York.

Forster, C., A. Stohl, P. James, and V. Thouret (2003), The residence times of aircraft emissions in the stratosphere using a mean emission inventory and emissions along actual flight tracks, *J. Geophys. Res.*, *108*, 8524, doi:10.1029/2002JD002515.

Frömming, C., M. Ponater, U. Burkhardt, A. Stenke, S. Pechtl, and R. Sausen (2011), Sensitivity of contrail coverage and contrail radiative forcing to selected key parameters, *Atmos. Env.*, *45*, 1483–1490, doi:10.1016/j.atmosenv.2010.11.033.

Fu, Q., B. Carlin, and G. Mace (2000), Cirrus horizontal inhomogeneity and OLR bias, *Geophys. Res. Lett.*, *27*, 3341–3344, doi:10.1029/2000GL011944.

Gierens, K., B. Kärcher, H. Mannstein, and B. Mayer (2009), Aerodynamic contrails: Phenomenology and flow physics, *J. Atmos. Sci.*, *66*, 217–226, doi:10.1175/2008JAS2767.

Graf, K., U. Schumann, H. Mannstein, and B. Mayer (2012), Aviation induced diurnal North Atlantic cirrus cover cycle, *Geophys. Res. Lett.*, *39*, L16804, doi:10.1029/2012GL052590.

Gultepe, I., and D. O. Starr (1995), Dynamical structure and turbulence in cirrus clouds: Aircraft observations during FIRE, *J. Atmos. Sci.*, *52*, 4159–4182.

Hagan, M. E., and J. M. Forbes (2002), Migrating and nonmigrating diurnal tides in the middle and upper atmosphere excited by tropospheric latent heat release, *J. Geophys. Res.*, *107*, 4754, doi:10.1029/2001JD001236.

Hagan, M. E., and J. M. Forbes (2003), Migrating and nonmigrating semidiurnal tides in the upper atmosphere excited by tropospheric latent heat release, *J. Geophys. Res.*, *108*, 1062, doi:10.1029/2002JA009466.

Harries, J. E., et al. (2005), The Geostationary Earth Radiation Budget project, *Bull. Amer. Meteor. Soc.*, *86*, 945–960, doi:10.1175/BAMS-86-7-945.

Haywood, J. M., R. P. Allan, J. Bornemann, P. M. Forster, P. N. Francis, S. Milton, G. Rädel, A. Rap, K. P. Shine, and R. Thorpe (2009), A case study of the radiative forcing of persistent contrails evolving into contrail-induced cirrus, *J. Geophys. Res.*, *114*, D24201, doi:10.1029/2009JD012650.

Hendricks, J., B. Kärcher, and U. Lohmann (2011), Effects of ice nuclei on cirrus clouds in a global climate model, *J. Geophys. Res.*, *116*, D18206, doi:10.1029/2010JD015302.

Hoinka, K., M. Reinhardt, and W. Metz (1993), North Atlantic air traffic within the lower stratosphere: Cruising times and corresponding emissions, *J. Geophys. Res.*, *98*, 23,113–23,131, doi:10.1029/93JD02262.

Huang, Y., V. Ramaswamy, and B. Soden (2007), An investigation of the sensitivity of the clear-sky outgoing longwave radiation to atmospheric temperature and water vapor, *J. Geophys. Res.*, *112*, D05104, doi:10.1029/2005JD006906.

Irvine, E. A., J. Hoskins, and K. P. Shine (2012), The dependence of contrail formation on the weather pattern and altitude in the North Atlantic, *Geophys. Res. Lett.*, *39*, L12802, doi:10.1029/2012GL051909.

Immler, F., R. Treffeisen, D. Engelbart, K. Krüger, and O. Schrems (2008), Cirrus, contrails, and ice supersaturated regions in high pressure systems at northern mid latitudes, *Atmos. Chem. Phys.*, *8*, doi:10.5194/acp-8-1689-2008.

Iwabuchi, H., P. Yang, K. N. Liou, and P. Minnis (2012), Physical and optical properties of persistent contrails: Climatology and interpretation, *J. Geophys. Res.*, *117*, D06215, doi:10.1029/2011JD017020.

Jensen, E. J., A. S. Ackermann, D. E. Stevens, O. B. Toon, and P. Minnis (1998), Spreading and growth of contrails in a sheared environment, *J. Geophys. Res.*, *103*, 13,557–13,567, doi:10.1029/98JD02594.

Jensen, E. J., et al. (2001), Prevalence of ice-supersaturated regions in the upper troposphere: Implications for optically thin ice cloud formation, *J. Geophys. Res.*, *106*, 17,253–17,266, doi:10.1029/2000JD900526.

Kärcher, B., B. Mayer, K. Gierens, U. Burkhardt, H. Mannstein, and R. Chatterjee (2009), Aerodynamic contrails: Microphysics and optical properties, *J. Atmos. Sci.*, *66*, 227–243, doi:10.1175/2008JAS2768.1.

Kärcher, B., U. Burkhardt, M. Ponater, and C. Frömming (2010), Importance of representing optical depth variability for estimates of global line-shaped contrail radiative forcing, *Proc. Natl. Acad. Sci. (USA)*, *19*(181–19), 184, doi:10.1073/pnas.1005555107.

Kennedy, J. J., P. Brohan, and S. F. B. Tett (2007), A global climatology of the diurnal variations in sea-surface temperature and implications for MSU temperature trends, *Geophys. Res. Lett.*, *34*, L05712, doi:10.1029/2006GL028920.

Kox, S. (2012), Remote sensing of the diurnal cycle of optically thin cirrus clouds. Ph.D. Thesis, University of Munich, Department of Physics.

Krebs, W., H. Mannstein, L. Bugliaro, and B. Mayer (2007), Technical note: A new day- and night-time Meteosat Second Generation Cirrus Detection Algorithm MeCiDA, *Atmos. Chem. Phys.*, *7*, 6145–6159, doi:10.5194/acp-7-6145-2007.

Lee, D. S., D. W. Fahey, P. M. Forster, P. J. Newton, R. C. N. Wit, L. L. Lim, B. Owen, and R. Sausen (2009), Aviation and global climate change in the 21st century, *Atmos. Env.*, *43*, 3520–3537, doi:10.1016/j.atmosenv.2009.04.024.

Liu, X., J. E. Penner, and M. Wang (2009), Influence of anthropogenic sulfate and black carbon on upper tropospheric clouds in the NCAR CAM3 model coupled to the IMPACT global aerosol model, *J. Geophys. Res.*, *114*, D03204, doi:10.1029/2008JD010492.

Loeb, N. G., B. A. Wielicki, D. R. Doelling, G. L. Smith, D. F. Keyes, S. Kato, N. Manalo-Smith, and T. Wong (2009), Toward optimal closure of the Earth's top-of-atmosphere radiation budget, *J. Climate*, *22*, 748–766, doi:10.1175/2008JCLI2637.1.

Mannstein, H., R. Meyer, and P. Wendling (1999), Operational detection of contrails from NOAA-AVHRR data, *Int. J. Rem. Sens.*, *20*, 1641–1660, doi:10.1080/014311699212650.

Mannstein, H., and U. Schumann (2005), Aircraft induced contrail cirrus over Europe, *Meteorol. Z.*, *14*(4), 549–554, doi:10.1127/0941-2948/2005/0058.

Mannstein, H., M. Vazquez-Navarro, K. Graf, D. P. Duda, and U. Schumann (2012), Contrail detection in satellite images, in Atmospheric Physics – Background, Methods, Trends, edited by U. Schumann, Springer, Berlin, Heidelberg, doi:10.1007/978-3-642-30183-4.

Marenco, A., et al. (1998), Measurement of ozone and water vapor by Airbus in-service aircraft: The MOZAIC airborne program. An overview, *J. Geophys. Res.*, *103*, 25631–25642, doi:10.1029/98JD00977.

Markowicz, K. M., and M. Witek (2011), Sensitivity study of global contrail radiative forcing due to particle shape, *J. Geophys. Res.*, *116*, D23203, doi:10.1029/2011JD016345.

Marquart, S., M. Ponater, F. Mager, and R. Sausen (2003), Future development of contrail cover, optical depth, and radiative forcing: Impacts of increasing air traffic and climate change, *J. Climate*, *16*, 2890–2904.

Mayer, B., and A. Kylling (2005), The libRadtran software package for radiative transfer calculations: Description and examples of use, *Atmos. Chem. Phys.*, *5*, 1855–1877, doi:10.5194/acp-5-1855-2005.

Meerkötter, R., U. Schumann, P. Minnis, D. R. Doelling, T. Nakajima, and Y. Tsushima (1999), Radiative forcing by contrails, *Ann. Geophysicae*, *17*, 1080–1094, doi:10.1007/s00585-999-1080-7.

Minnis, P., D. F. Young, D. P. Garber, L. Nguyen, W. L. Smith Jr., and R. Palikonda (1998), Transformation of contrails into cirrus during SUCCESS, *Geophys. Res. Lett.*, *25*, 1157–1160, doi:10.1029/97GL03314.

Minnis, P., U. Schumann, D. R. Doelling, K. Gierens, and D. W. Fahey (1999), Global distribution of contrail radiative forcing, *Geophys. Res. Lett.*, *26*, 1853–1856, doi:10.1029/1999GL900358.

Minnis, P., J. K. Ayers, R. Palikonda, and D. Phan (2004), Contrails, cirrus trends, and climate, *J. Clim.*, *17*, 1671–1685.

Minnis, P., R. Palikonda, B. J. Walter, J. K. Ayers, and H. Mannstein (2005), Contrail properties over the eastern North Pacific from AVHRR data, *Meteor. Z.*, *14*, 515–523, doi:10.1127/0941-2948/2005/0056.

Morcrette, J.-J., H. W. Barker, J. N. S. Cole, M. J. Iacono, and R. Pincus (2008), Impact of a new radiation package, McRad, in the ECMWF Integrated Forecasting System, *Mon. Wea. Rev.*, *136*, 4773–4798, doi:10.1175/2008MWR2363.1.

Myhre, G., and F. Stordal (2001), On the tradeoff of the solar and thermal infrared impact of contrails, *Geophys. Res. Lett.*, *28*, 3119–3122, doi:10.1029/2001GL013193.

Myhre, G., et al. (2009), Intercomparison of radiative forcing calculations of stratospheric water vapour and contrails, *Meteor. Z.*, *18*, 585–596, doi:10.1127/0941-2948/2009/0411.

Ovarlez, J., J. F. Gayet, K. Gierens, J. Ström, H. Ovarlez, F. Auriol, R. Busen, and U. Schumann (2002), Water vapor measurements inside cirrus clouds in Northern and Southern hemispheres during INCA, *Geophys. Res. Lett.*, *29*, 60–1–60–4, doi:10.1029/2001gl014440.

Palikonda, R., P. Minnis, D. P. Duda, and H. Mannstein (2005), Contrail coverage derived from 2001 AVHRR data over the continental United States of America and surrounding areas, *Meteor. Z.*, *14*, 525–536, doi:10.1127/0941-2948/2005/0051.

Penner, J. E., Y. Chen, M. Wang, and X. Liu (2009), Possible influence of anthropogenic aerosols on cirrus clouds and anthropogenic forcing, *Atmos. Chem. Phys.*, *9*, 879–896, doi:10.5194/acp-9-879-2009.

Ponater, M., S. Marquart, and R. Sausen (2002), Contrails in a comprehensive global climate model: Parameterization and radiative forcing results, *J. Geophys. Res.*, *107*, 4164, doi:10.1029/2001JD000429.

Rädel, G., and K. P. Shine (2008), Radiative forcing by persistent contrails and its dependence on cruise altitudes, *J. Geophys. Res.*, *113*, D07105, doi:10.1029/2007JD009117.

Rap, A., P. M. Forster, A. Jones, O. Boucher, J. M. Haywood, N. Bellouin, and R. R. De Leon (2010), Parameterization of contrails in the UK Met Office Climate Model, *J. Geophys. Res.*, *115*, D10205, doi:10.1029/2009JD012443.

Sausen, R., K. Gierens, M. Ponater, and U. Schumann (1998), A diagnostic study of the global distribution of contrails. Part I: Present day climate, *Theor. Appl. Clim.*, *61*, 127–141, doi:10.1007/s007040050058.

Sausen, R., et al. (2005), Aviation radiative forcing in 2000: An update on IPCC (1999), *Meteor. Z.*, *14*, 555–561, doi:10.1127/0941-2948/2005/0049.

Schmetz, J., P. Pili, S. Tjemkes, D. Just, J. Kerkmann, S. Rota, and A. Ratier (2002), An introduction to Meteosat Second Generation (MSG), *Bull. Amer. Meteor. Soc.*, *83*, 977–992, doi:10.1175/BAMS-83-7-Schmetz-2.

Schulz, J., et al. (2009), Operational climate monitoring from space: The EUMETSAT Satellite Application Facility on Climate Monitoring (CM-SAF), *Atmos. Chem. Phys.*, *9*, 1687–1709, doi:10.5194/acp-9-1687-2009.

Schumann, U. (2012), A contrail cirrus prediction model, *Geosci. Model Dev.*, *5*, 543–580, doi:10.5194/gmd-5-543-2012.

Schumann, U., and P. Wendling (1990), Determination of contrails from satellite data and observational results, in Air Traffic and the Environment – Background, Tendencies and Potential Global Atmospheric Effects, edited by Schumann, U., pp. 138–153, Springer.

Schumann, U., B. Mayer, K. Graf, and H. Mannstein (2012), A parametric radiative forcing model for contrail cirrus, *J. Appl. Meteor. Climatol.*, *51*, 1391–1406, doi:10.1175/JAMC-D-11-0242.1.

Slingo, A., K. I. Hodges, and G. J. Robinson (2004), Simulation of the diurnal cycle in a climate model and its evaluation using data from Meteosat 7, *Quart. J. Roy. Meteor. Soc.*, *130*, 1449–1467, doi:10.1256/qj.03.165.

Smith, G. L., and D. A. Rutan (2003), The diurnal cycle of outgoing longwave radiation from Earth Radiation Budget Experiment measurements, *J. Atmos. Sci.*, *60*, 1529–1542, doi:10.1175/2997.1.

Smith, G. L., P. E. Mlynczak, D. A. Rutan, and T. Wong (2008), Comparison of the diurnal cycle of outgoing longwave radiation from a climate model with results from ERBE, *J. Appl. Meteor. Climatol.*, *47*, 3188–3201, doi:10.1175/2008JAMC1924.1.

Stordal, F., G. Myhre, E. J. G. Stordal, W. B. Rossow, D. S. Lee, W. Arlander, and T. Svendby (2005), Is there a trend in cirrus cloud cover due to aircraft traffic?, *Atmos. Chem. Phys.*, *5*, 2155–2162, doi:10.5194/acp-5-2155-2005.

Stubenrauch, C. J., and U. Schumann (2005), Impact of air traffic on cirrus coverage, *Geophys. Res. Lett.*, *32*, L14,813, doi:10.1029/2005GL022707.

Stubenrauch, C. J., A. Chedin, G. Rädel, N. A. Scott, and S. Serrar (2006), Cloud properties and their seasonal and diurnal variability from TOVS path-B, *J. Climate*, *19*, 5531–5553, doi:10.1175/JCLI3929.1.

Stubenrauch, C. J., S. Cros, A. Guignard, and N. Lamquin (2010), A 6-year global cloud climatology from the Atmospheric InfraRed Sounder AIRS and a statistical analysis in synergy with CALIPSO and CloudSat, *Atmos. Chem. Phys.*, *10*, 7197–7214, doi:10.5194/acp-10-7197-2010.

Stuber, N., and P. Forster (2007), The impact of diurnal variations of air traffic on contrail radiative forcing, *Atmos. Chem. Phys.*, *7*, 3153–3162, doi:10.5194/acp-7-3153-2007.

Tompkins, A., K. Gierens, and G. Rädel (2007), Ice supersaturation in the ECMWF Integrated Forecast System, *Quart. J. Roy. Meteor. Soc.*, *133*, 53–63, doi:10.1002/qj.14.

Trenberth, K. E., J. T. Fasullo, and J. Kiehl (2009), Earth's global energy budget, *Bull. Amer. Meteor. Soc.*, *90*, 311–323, doi:10.1175/2008BAMS2634.1.

Vazquez-Navarro, M. (2009), Life cycle of contrails from a time series of geostationary satellite images, Ph.D. thesis, University of Munich, Department of Physics.

Vazquez-Navarro, M., H. Mannstein, and B. Mayer (2010), An automatic contrail tracking algorithm, *Atmos. Meas. Tech.*, *3*, 1089–1101, doi:10.5194/amt-3-1089-2010.

Vazquez-Navarro, M., B. Mayer, and H. Mannstein (2012), A fast method for the retrieval of integrated longwave and shortwave top-of-atmosphere irradiances from MSG/SEVIRI (RRUMS), *Atmos. Meas. Tech. Discuss.*, *5*, 4969–5008, doi:10.5194/amtd-5-4969-2012.

Wilcox, L. J., B. J. Hoskins, and K. P. Shine (2012), A global blended tropopause based on ERA data. Part I: Climatology, *Quart. J. Roy. Meteor. Soc.*, *138*, 561–575, doi:10.1002/qj.951.

Wilkerson, J. T., M. Z. Jacobson, A. Malwitz, S. Balasubramanian, R. Wayson, G. Fleming, A. D. Naiman, and S. K. Lele (2010), Analysis of emission data from global commercial aviation: 2004 and 2006, *Atmos. Chem. Phys.*, *10*, 6391–6408, doi:10.5194/acp-10-6391-2010.

Winker, D. M., et al. (2010), The CALIPSO mission – A global 3d view of aerosols and clouds, *Bull. Amer. Meteor. Soc.*, *91*, 1211–1229, doi:10.1175/2010BAMS3009.1.

Wylie, D. (2008), Diurnal cycles of clouds and how they affect polar-orbiting satellite data, *J. Climate*, *21*, 3989–3996, doi:10.1175/2007JCLI2027.1.

Zerefos, C., K. Eleftheratos, D. Balis, P. Zanis, G. Tselioudis, and C. Meleti (2003), Evidence of impact of aviation on cirrus cloud formation, *Atmos. Chem. Phys.*, *3*, 1633–1644, doi:10.5194/acp-3-1633-2003.